Shen Y, Freddi F, Li Y, Li J. Parametric experimental investigation of unbonded post-tensioned reinforced concrete bridge piers under cyclic loading. Earthquake Engng Struct Dyn. https://doi.org/10.1002/eqe.3732

Parametric experimental investigation of unbonded post-tensioned reinforced concrete bridge piers under cyclic loading

Yu Shen[a], Fabio Freddi[b], Yongxing Li[c], Jianzhong Li[a,*]

[a] *State Key Laboratory of Disaster Reduction in Civil Engineering, Tongji University, Shanghai 200092, China.*
[b] *Dept. of Civil, Environmental & Geomatic Engineering, University College London, London WC1E 6BT, U.K.*
[c] *Civil Engineering (Bridge, Tunnel & Subgrade) Design Research Inst., China Railway Design Corp., Tianjin 300308, China.*
[*]Corresponding Author. Tel.: +86 (21) 65980455. E-mail address: lijianzh@tongji.edu.cn (J. Li)

ABSTRACT

The present paper investigates the cyclic performance of unbonded post-tensioned reinforced concrete (PRC) rocking piers by a parametric experimental campaign. PRC rocking specimens are assembled by hybrid connections, containing an ungrouted post-tensioned (PT) bar and grouted mild steel bars, *i.e.*, energy-dissipation (ED) components. The properties of a benchmark PRC pier were defined according to a design procedure to control its strength, ductility, energy dissipation capacity, and self-centering behavior. Five additional PRC piers with different ED bars amounts, initial PT force, and ED bars unbonded lengths were also tested to investigate the influence of these parameters on the cyclic performance. The test results show the superior cyclic performance of the PRC pier in limiting both damage and residual deformations. The parametric analysis highlighted that decreasing the initial PT force and/or ED bars amount enhances the PRC's ED capacity at the expense of the lateral force resistance and self-centering behavior. Moreover, it has been observed that the influence of ED bars' unbonded length only minimally affects the PRC pier's cyclic performance due to ED bars' bond-slip and concrete cover spalling of the pier shaft. Analytical models describing the PRC piers' lateral force-drift cyclic behavior were formulated and calibrated, showing a good agreement with test results for all specimens. The results and findings provide a valuable reference and solution for tailoring an efficient parameter recommendation of PRC rocking piers.

Keywords: Rocking; self-centering; post-tensioning reinforced concrete bridge piers; seismic design; experimental testing; parametric analysis.

1. INTRODUCTION

Reinforced concrete (RC) bridge piers are conventionally designed to exhibit large inelastic deformations under moderate-to-strong earthquakes with consequent damage to the structural members and large residual drifts.[1-3] This damage results in direct and indirect losses such as repair costs and costly downtime during the reparation process when the bridge is not functional. Traffic closure for the assessment, repair, or demolition and reconstruction of damaged bridges is inevitable with conventional technologies, and the corresponding economic losses are often significant.[4] One of the most well-known examples is the Kobe earthquake in 1995, where over one hundred RC bridges were demolished due to excessive permanent drifts.[5] In this context, there is an urgent societal need for innovative structural solutions that can effectively achieve seismic resilience, mitigating disruptions to the traveling public.[4, 6-8]

A typology of resilient bridges is obtained using self-centering rocking piers,[8-17] where unbonded post-tensioned (PT) elements and energy dissipation (ED) components are combined within precast elements. The PT elements provide the self-centering capability, while the ED components aim to increase the structure's dissipation capacity.[10] It has been demonstrated that this solution can allow minimal damage to the bridge pier even after significant seismic events due to the inherent rocking isolation[7, 9], thus promoting seismic resilience. These merits attracted the interest of engineers and researchers over the past two decades. Mander and Cheng[15] conducted a pioneering study on the application of this technology, developing a design philosophy and experimentally evaluating its validity. Kwan and Billington[18, 19] and Ou *et al.*[14] proposed the use of precast unbonded post-tensioned reinforced concrete (PRC) bridge piers and segment PRC bridge piers, respectively, and analytically assessed their cyclic performance, showing potential advantages and applications in seismic regions. The intrinsic flag-shape hysteretic behavior of the PRC bridge pier makes this system possess ED capacity while preserving small residual deformation.[14] The experimental comparison between the PRC columns and an RC monolithic benchmark confirmed the seismic superiority of such a hybrid system with negligible residual drift and limited damage.[9, 16, 20] Faster precast construction processes and lower material costs are additional benefits highlighted by these research studies. These encouraging outcomes from previous work led to many follow-up investigations into precast rocking piers, including exploration of viable construction methods,[12, 21] enhanced ED solutions,[10, 22] advanced simulation techniques,[8, 23, 24] and realistic load testing scenarios.[23-27]

The amount of ED and the level of initial PT force in the PT rocking pier are two key design parameters, and their combination needs to be carefully proportioned to optimize the self-centering and ED capacity of the system.[23, 28-30] It is noteworthy that the PT elements and ED devices have conflicting effects. In fact, the ED elements provide additional strength, stiffness, and dissipation capacity producing beneficial effects in terms of peak drifts reduction; however, after experiencing the post-elastic behavior, they can generate forces that oppose displacements toward zero drift.[12, 31, 32] In this context, several research studies investigated the optimum combination of ED devices and PT force on the seismic response of PT hybrid rocking columns; however, these studies are often limited to numerical simulations.[17, 28, 29, 31-35] Li *et al.*[31, 33] performed analytical studies on the quasi-static and dynamic response of unbonded PRC rocking piers considering several configurations varying both the initial PT forces and amounts of ED bars. Roh *et al.*[34] performed a similar study focusing mainly on the effects of the properties of ED bars. Hieber *et al.*[17] examined the influence of pier aspect ratio, longitudinal ED ratio, and axial-load ratio by monotonic pushover analyses and dynamic earthquake analyses. Similar numerical studies have also been carried out by Chou *et al.*[29], Nikbakht *et al.*[35], and Ou[36] while focusing on precast segment PRC bridge piers. However, only a few experimental studies have been performed in this research direction to accurately determine the influences of PT forces and the amount of ED bars. Bu *et al.*[30] and Zhang *et al.*[37] performed cyclic experimental tests on PRC piers investigating the influence of the axial force and reinforcements' arrangements. Additional experimental tests were conducted by Fathi *et al.*[38] to investigate the influence of initial PT force, ED bars amount, and construction method for PRC piers.

Apart from the amount of ED bars, their bonded/unbonded condition at the rocking joint is also a concern in PRC rocking piers because it may affect the stiffness and the deformation capacity of the system, which could be affected by premature fracture of ED bars.[12, 14, 30, 39] Moreover, previous experimental tests on post-tensioned concrete-filled steel tube (PCFT) conducted by the authors[12, 13] highlighted the influence of the strain penetration occurring along ED bars, and thus the bars slip. This phenomenon potentially contributes to the withdrawal of the unbonded portion design (*i.e.*, keep bonded) in the ED bars and, if properly considered, could facilitate the construction process. However, additional experimental evidence is required in this direction.

Although the aforementioned research works demonstrated the feasibility of the proposed technology and significantly contributed to the design and construction strategies for PRC bridge piers, further research is needed to define optimized solutions and design methodologies. In addition, there is a significant need for advanced studies in order to reflect the academic research in policymaking and building codes. The present paper introduces the experimental campaign performed on six PRC bridge piers subjected to quasi-static cyclic loading considering the influence of initial PT forces and amounts/bonded state of ED bars. A PRC bridge pier was designed according to the specified performance objectives (*i.e.*, the benchmark PRC bridge pier), and five additional PRC versions were further detailed by varying the initial PT force, the amount of ED bars, or their unbonded length. All piers were experimentally assessed, considering their cyclic global and local responses. In addition, analytical equations describing the cyclic behavior of PRC piers were presented and calibrated against the test results. The objectives of the present study are *1)* to validate the cyclic performance of the PRC pier against the considered design objectives; *2)* to identify the effects of varying the PT force and ED bars amount; *3)* to identify the effects of the unbonded length of ED bars; and *4)* to develop and validate a simple analytical model that can capture the cyclic behavior of PRC piers.

The paper is organized as follows: *Section 2* defines the analytical formulation for the force-displacement behavior of PRC piers and discusses tailored design criteria; *Section 3* describes the experimental campaign, including the design of the test specimens, coupon tests characterizing the materials' properties, and the loading protocol; *Section 4* describes the damage observations and the general cyclic behavior and PT bar response while *Section 5* comprehensively evaluates the effects of the variables of interest on the PRC cyclic performance; and based on the test observations and results, the presented analytical equations for predicting cyclic behavior are calibrated in *Section 6*.

2. POST-TENSIONED REINFORCED CONCRETE (PRC) PIER AND DESIGN

Figure 1(A) shows the investigated PRC pier, including the unbonded PT bar at the center of the pier cross-section and ED bars composed of reinforcement mild steel anchored in grouted corrugated ducts. This combination is expected to provide the self-centering capacity through the elastic response of the PT bar and energy dissipation capacity by yielding of the ED bars. A layer of mortar bed, with sufficient integrity capacity, is included beneath the pier bottom to guarantee a well-leveled footing surface and seal the base joint preventing steel corrosion.[40] Typically, ED bars are characterized by an unbonded length at the pier-mortar bed interface to avoid strain concentrations due to rocking.

2.1 Force-displacement relationship

Figure 1(B) shows the typical flag-shape hysteretic curve expected in PRC piers. The seismic-induced displacement demand is controlled by the rocking behavior at the pier base and the elastic deformation of the pier body. At the end of the seismic excitation, the PRC pier returns to the original position (*i.e.*, no residual displacement) thanks to the recentering PT force. Figure 1(C) shows the cyclic force-displacement (F-Δ) behavior and the key points characterizing its response. This is characterized by two phases: the closed phase (*i.e.*, points 0 to 1 and 6 to7); and the gap-opening phase (*i.e.*, points 2 to 6). Point 1 corresponds to the decompression (*i.e.*, gap-opening) of the pier base and the beginning of the PT bar and ED bars elongation (*i.e.*, point 2). Points 3 and 5 indicate the onset of tension and compression yielding of the ED bars during loading and unloading, respectively. Point 6 represents the gap-closing phase during unloading, while points 4 and 7 represent the maximum (*i.e.*, target) and the zero displacements of the pier, respectively.

2.1.1 Pre-rocking gap-closed phase

The closed phase is characterized by an almost rigid response of the pier base and the elastic deformation of the pier shaft [Figure 2(A)]. At the decompression state (*i.e.*, point 1), the stress in the concrete fiber furthest from the rocking toe becomes zero [Figure 2(B)], and linear concrete stress distribution is developed at the pier base with the maximum value σ_{cm_dec} at the rocking toe. Being x the distance from the center of the cross-section, the concrete stress $\sigma_{cm}(x)$ can be expressed as:

$$\sigma_{cm}(x) = \frac{\sigma_{cm\_dec}}{d} \times (x + \frac{d}{2}) \tag{1}$$

where d is the diameter of the pier cross-section. The equilibrium of vertical forces acting on the base section can be used to calculate the σ_{cm_dec} as follow:

$$F_G + F_{PT\_ini} = \int_{-d/2}^{d/2} 2 \times \sigma_{cm}(x) \times \sqrt{(\frac{d}{2})^2 - x^2}\, dx \quad \rightarrow \quad \sigma_{cm\_dec} = \frac{8 \times (F_G + F_{PT\_ini})}{d^2 \pi} \tag{2}$$

where F_G and F_{PT_ini} are the axial gravity load from the superstructure and the initial post-tensioning force in the PT bar, respectively. Thus, the decompression moment M_1, decompression force F_1, and corresponding lateral displacement Δ_1 at the bridge pier top point can be determined as follow:

$$M_1 = \int_{-d/2}^{d/2} 2 \times \sigma_{cm}(x) \times x \sqrt{(d/2)^2 - x^2}\, dx \qquad F_1 = \frac{M_1}{h + \frac{F_G + F_{PT\_ini}}{k_E}} = \frac{k_E d \times (F_G + F_{PT\_ini})}{8(F_G + F_{PT\_ini} + k_E h)} \qquad \Delta_1 = \frac{F_1}{k_E} \tag{3}$$

where h and k_E are, respectively, the height and elastic stiffness of the bridge pier.

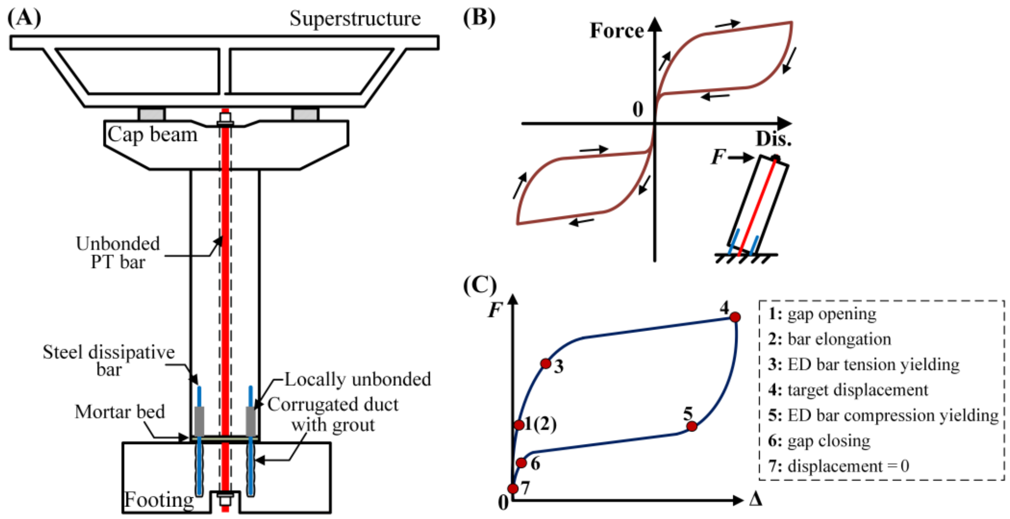

FIGURE 1 Typical PRC pier: (A) Conceptual configuration; (B) force-displacement behavior; and (C) key points in the hysteretic loop.

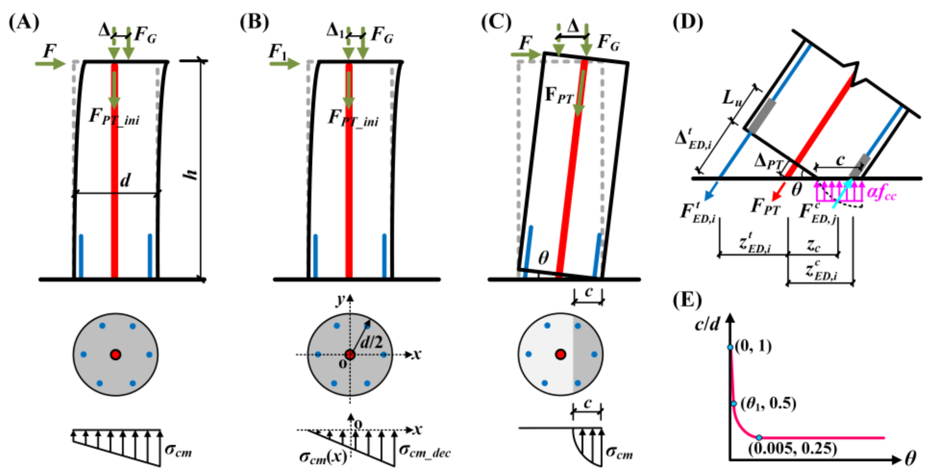

FIGURE 2 PRC pier subjected to the lateral loads: (A) Gap-closed phase; (B) decompression state; (C) gap-opening phase; (D) forces developed at the rocking base; and (E) three-stage idealization of the neutral axis depth.

2.1.2 Gap-opening rocking phase

Exceeding point 1, the base gap-opening emerges (*i.e.*, base toe uplift), and a base rotation θ is observed [Figures 2(C) and (D)]. For convenience of interpretation, the rotation at point 1 is defined as $\theta_1 = \Delta_1/h$. It is noteworthy that this is the chord rotation related to the displacement at the bridge pier top point. Once the rocking behavior is activated [point 2 in Figure 1(C)], there is an evolution of the neutral axis depth c, and hence of the ratio c/d, as shown in Figure 2(E). The neutral axis depth c is assumed to be located at the mid-depth of the cross-section (*i.e.*, $c/d = 0.5$) for the initial rocking state of $\theta = \theta_1$. Successively, with the increase of θ, the neutral axis depth c decreases until $\theta = 0.005$, beyond which the ratio c/d does not significantly vary according to previous experimental and numerical results.[41-44] At this critical rotation, the ratio c/d can be approximately assumed equal to 0.25.[40] Combining this observation with the initial rocking state, a simplified piecewise relationship between the ratio c/d and the base rotation θ can be introduced as follows:

$$\frac{c}{d} = \begin{cases} 1 - k\theta & \theta \le \theta_1 \quad (k = 0.5/\theta_1) \\ \dfrac{A}{\theta} + B & \theta_1 < \theta < 0.005 \quad (A = \dfrac{0.005\theta_1}{0.02 - 4\theta_1};\ B = \dfrac{0.005 - 2\theta_1}{0.02 - 4\theta_1}) \\ 0.25 & \theta \ge 0.005 \end{cases} \tag{4}$$

where a linear relationship, a power function, and a constant value are defined for the pre-rocking phase, the rocking phase with $\theta < 0.005$, and the rocking phase with $\theta \ge 0.005$, respectively. The adequacy of this simplified relationship is validated against the experimental results in *Section 5*. Note that based on Eq.s (4), the conventionally used iterative process to determine the neutral axis depth c that satisfies the vertical force equilibrium at a given θ[33, 42, 45] is not required, and the proposed procedure allows directly calculating the lateral force of the PRC pier during rocking.

It is noteworthy that the following formulation assumes the PT bar to behave elastically while the ED bars are assumed to be elastic perfectly plastic. The forces in the PT bar (F_{PT}) and ED bars in tension, identified by the subscript i ($F^t_{ED,i}$), are respectively given by the following Eq.s (5) and (6) [see Figure 2(D)]:

$$F_{PT} = F_{PT\_ini} + A_{PT}E_{PT} \times \frac{\Delta_{PT}}{L_{PT}} \qquad \Delta_{PT} = (\frac{d}{2} - c)\theta \tag{5}$$

$$F^t_{ED,i} = \begin{cases} A_{ED}E_{ED}\dfrac{\Delta^t_{ED,i}}{L_u + 2L_{eu}} & \text{for } \dfrac{\Delta^t_{ED,i}}{L_u + 2L_{eu}} \le \varepsilon_{y\_ED};\ \text{loading} \\ A_{ED}f_{y\_ED} & \text{for } \dfrac{\Delta^t_{ED,i}}{L_u + 2L_{eu}} > \varepsilon_{y\_ED};\ \text{loading} \\ A_{ED}(f_{y\_ED} + E_{ED}\dfrac{\Delta^t_{ED,i} - \Delta^t_{ED\_4,i}}{L_u + 2L_{eu}}) & \text{for } \dfrac{\Delta^t_{ED,i} - \Delta^t_{ED\_4,i}}{L_u + 2L_{eu}} > \text{-}2\varepsilon_{y\_ED};\ \text{unloading} \\ \text{-}A_{ED}f_{y\_ED} & \text{for } \dfrac{\Delta^t_{ED,i} - \Delta^t_{ED\_4,i}}{L_u + 2L_{eu}} \le \text{-}2\varepsilon_{y\_ED};\ \text{unloading} \end{cases} \qquad \Delta^t_{ED,i} = (z^t_{ED,i} + \frac{d}{2} - c)\theta \tag{6}$$

where L_{PT}, A_{PT}, and E_{PT} are respectively the length, cross-sectional area, and Young modulus of the PT bar; Δ_{PT} is the elongation of the PT bar at rotation θ; L_u, A_{ED}, ε_{y_ED}, f_{y_ED}, and E_{ED} are respectively the designed unbonded length, cross-sectional area, yielding strain, yielding stress, and Young modulus of the ED bars; $\Delta^t_{ED,i}$ and $\Delta^t_{ED\_4,i}$ are the elongation of the i^{th} ED bar at rotation θ and target rotation θ_4 [Figure 1(C)], respectively; $z^t_{ED,i}$ is the distance of the i^{th} ED bar from the center of the cross-section; and L_{eu} is the additional equivalent unbonded length in ED bars developed due to the strain penetration,[46] assumed equal to four times the bar diameter.[39] The force in each ED bar in compression, identified by the subscript j ($F^c_{ED,j}$), can be obtained based on the 'Monolithic Beam Analogy'[45] as follows:

$$F^c_{ED,j} = \begin{cases} A_{ED}E_{ED} \times \varepsilon^c_{ED,j} & \text{for } \varepsilon^c_{ED,j} \le \varepsilon_{y\_ED};\ \text{loading} \\ A_{ED}f_{y\_ED} & \text{for } \varepsilon^c_{ED,j} > \varepsilon_{y\_ED};\ \text{loading} \\ A_{ED}[f_{y\_ED} + E_{ED}(\varepsilon^c_{ED,j} - \varepsilon^c_{ED\_4,j})] & \text{for } \varepsilon^c_{ED,j} - \varepsilon^c_{ED\_4,j} \le \text{-}2\varepsilon_{y\_ED};\ \text{unloading} \\ \text{-}A_{ED}f_{y\_ED} & \text{for } \varepsilon^c_{ED,j} - \varepsilon^c_{ED\_4,j} > \text{-}2\varepsilon_{y\_ED};\ \text{unloading} \end{cases} \qquad \varepsilon^c_{ED,j} = \frac{\theta}{L_p} \times [z^c_{ED,j} - (\frac{d}{2} - c)] \tag{7}$$

where $\varepsilon^{c}_{ED,j}$ and $\varepsilon^{c}_{ED\_4,j}$ are the strain of the j^{th} ED bar at rotation θ and target rotation θ_4, respectively; $z^{c}_{ED,j}$ is the distance of the j^{th} ED bar from the center of the cross-section; and L_p is the plastic hinge length of the monolithic analog. Assuming a uniform concrete compressive stress with a value of αf_{cc} acting at the pier base over the neutral axis depth c is possible to derive the concrete compression resultant C_c, as shown in Figure 2(D), where f_{cc} is the confined concrete strength, and α is the equivalent rectangular block parameter related to the rotation θ and obtained by the equilibrium of the vertical forces acting on the base section as follows:

$$C_c = \alpha f_{cc} A^{c}_{con} = F_G + (F_{PT} + \sum F^{t}_{ED,\,i} - \sum F^{c}_{ED,\,j})\cos\theta \quad \rightarrow \quad \alpha(\theta) = \frac{F_G + (F_{PT} + \sum F^{t}_{ED,\,i} - \sum F^{c}_{ED,\,j})\cos\theta}{f_{cc} A^{c}_{con}} \tag{8}$$

where A^{c}_{con} is the area of the compressive concrete over the neutral axis depth.

Considering the variability of the ratio c/d defined by Eq.s (4), and the contribution of individual components defined by Eq.s (5) to (8), the moment about the center of the cross-section for the rotation θ is given by:

$$M(\theta) = \sum_{i=1}^{N^{t}_{ED}} (F^{t}_{ED,i}\cos\theta \times z^{t}_{ED,i}) + \sum_{j=1}^{N^{c}_{ED}} (F^{c}_{ED,j}\cos\theta \times z^{c}_{ED,j}) + \alpha f_{cc} A^{c}_{con} \times z_c \tag{9}$$

where N^{t}_{ED} and N^{c}_{ED} are respectively the number of the tension and compression ED bars; and z_c is the location of the resultant C_c from the center of the cross-section. Specifically, from points 2 to 4 in Figure 1(C), $M(\theta)$ is given by:

$$M_{2\text{-}3}(\theta) = \sum_{i=1}^{N^{t}_{ED}} (A_{ED} E_{ED} \frac{\Delta^{t}_{ED,i}}{L_u + 2L_{eu}} \times z^{t}_{ED,i})\cos\theta + \sum_{j=1}^{N^{c}_{ED}} (A_{ED} E_{ED} \varepsilon^{c}_{ED,j} \times z^{c}_{ED,j})\cos\theta + \alpha f_{cc} A^{c}_{con} \times z_c \tag{10a}$$

$$\begin{aligned} M_{3\text{-}4}(\theta) = & \sum_{i=1}^{N^{t}_{ED}-n^{t}_{ED}} (A_{ED} E_{ED} \frac{\Delta^{t}_{ED,i}}{L_u + 2L_{eu}} \times z^{t}_{ED,i})\cos\theta + \sum_{i=1}^{n^{t}_{ED}} (A_{ED} f_{y\_ED} \times z^{t}_{ED,i})\cos\theta + \\ & + \sum_{j=1}^{N^{c}_{ED}-n^{c}_{ED}} (A_{ED} E_{ED} \varepsilon^{c}_{ED,j} \times z^{c}_{ED,j})\cos\theta + \sum_{j=1}^{n^{c}_{ED}} (A_{ED} f_{y\_ED} \times z^{c}_{ED,j})\cos\theta + \alpha f_{cc} A^{c}_{con} \times z_c \end{aligned} \tag{10b}$$

where n^{t}_{ED} and n^{c}_{ED} are respectively the number of yielding ED bars in tension and compression, which needs to be identified for each θ value. Based on Eq.s (4), (6), and (10a), the rotation θ_3, corresponding to the first yielding of the ED bars in tension, and the corresponding moment M_3 are given by:

$$\theta_3 = \frac{\varepsilon_{y\_ED} \times (L_u + 2L_{eu})}{d \times (1 - c/d)} \qquad M_3 = M_{2\text{-}3}(\theta_3) \tag{11}$$

Assuming that all ED bars in tension are yielded at rotation θ_4, the corresponding moment M_4 is given by:

$$M_4 = \sum_{i=1}^{N^{t}_{ED}} (A_{ED} f_{y\_ED} \times z^{t}_{ED,i})\cos\theta + \sum_{j=1}^{N^{c}_{ED}-n^{c}_{ED}} (A_{ED} E_{ED} \varepsilon^{c}_{ED,j} \times z^{c}_{ED,j})\cos\theta + \sum_{j=1}^{n^{c}_{ED}} (A_{ED} f_{y\_ED} \times z^{c}_{ED,j})\cos\theta + \alpha f_{cc} A^{c}_{con} \times z_c \tag{12}$$

Upon rocking unloading from target point 4 to the gap-closed at point 6 [Figure 1(C)], the $M(\theta)$ curve follows a path made of segments parallel to and of the same length as the previous loading segments and their opposite-direction counterparts (*i.e.*, from point 2 to 4). Specifically, from points 4 to 5 and 5 to 6 in Figure 1(C), $M(\theta)$ is given by:

$$\begin{aligned} M_{4\text{-}5}(\theta) = & \sum_{i=1}^{N^{t}_{ED}} [A_{ED} (f_{y\_ED} + E_{ED} \frac{\Delta^{t}_{ED,i} - \Delta^{t}_{ED\_4,i}}{L_u + 2L_{eu}}) \times z^{t}_{ED,i}]\cos\theta + \\ & + \sum_{j=1}^{N^{c}_{ED}-n^{c}_{ED}} (A_{ED} E_{ED} \varepsilon^{c}_{ED,j} \times z^{c}_{ED,j})\cos\theta + \sum_{j=1}^{n^{c}_{ED}} \left\{ A_{ED} [f_{y\_ED} + E_{ED} (\varepsilon^{c}_{ED,j} - \varepsilon^{c}_{ED\_4,j})] \times z^{c}_{ED,j} \right\} \cos\theta + \alpha f_{cc} A^{c}_{con} \times z_c \end{aligned} \tag{13a}$$

$$\begin{aligned} M_{5\text{-}6}(\theta) = & \sum_{i=1}^{N^{t}_{ED}-n^{t}_{ED}} [A_{ED} (f_{y\_ED} + E_{ED} \times \frac{\Delta^{t}_{ED,i} - \Delta^{t}_{ED\_4,i}}{L_u + 2L_{eu}}) \times z^{t}_{ED,i}]\cos\theta + \sum_{i=1}^{n^{t}_{ED}} (\text{-}A_{ED} f_{y\_ED} \times z^{t}_{ED,i})\cos\theta + \\ & + \sum_{j=1}^{N^{c}_{ED}-n^{c}_{ED}} \left\{ A_{ED} [f_{y\_ED} + E_{ED} (\varepsilon^{c}_{ED,j} - \varepsilon^{c}_{ED\_4,j})] \times z^{c}_{ED,j} \right\} \cos\theta + \sum_{j=1}^{n^{c}_{ED}} (A_{ED} f_{y\_ED} \times z^{c}_{ED,j})\cos\theta + \alpha f_{cc} A^{c}_{con} \times z_c \end{aligned} \tag{13b}$$

Based on Eq.s (4), (6), and (13a), the rotation θ_5, corresponding to the first yielding of the ED bars in compression under the reverse loading, and the corresponding moment M_5 is given by:

$$\theta_5 = \frac{\Delta^t_{ED\_4} - 2\varepsilon_{y\_ED} \times (L_u + 2L_{eu})}{d \times (1 - c/d)} \qquad M_5 = M_{4\text{-}5}(\theta_5) \tag{14}$$

Assuming that all ED bars yield in compression at θ_6 and neglecting the effect of elastic ED bars leads to M_6 being derived from Eq. (13b) as:

$$M_6 = \sum_{i=1}^{N^t_{ED}} (\text{-}A_{ED} f_{y\_ED} \times z^t_{ED,i}) \cos\theta + \sum_{j=1}^{N^c_{ED} - n^c_{ED}} \left\{ A_{ED}[f_{y\_ED} + E_{ED}(\varepsilon^c_{ED,j} - \varepsilon^c_{ED\_4,j})] \times z^c_{ED,j} \right\} \cos\theta + \alpha f_{cc} A^c_{con} \times z_c \tag{15}$$

Note that the $\theta_6 = \theta_1$.

The lateral force F and the top displacement of PRC pier Δ can be accordingly calculated as:

$$F = \frac{M(\theta)}{h} \qquad \Delta = \Delta_e(\theta) + \Delta_r(\theta) + \Delta_s(\theta) = \frac{F(\theta)}{k_e} + \theta h + \frac{F(\theta)h}{GA_g} \tag{16}$$

where $\Delta_e(\theta)$, $\Delta_r(\theta)$, and $\Delta_s(\theta)$ are respectively the lateral displacements induced by the flexural deformation, rocking behavior, and shear force at the rotation θ; G and A_g are the shear modulus and gross cross-sectional area of the PRC pier.

2.1.3 Post-rocking gap-closed phase

From points 6 to 7, corresponding to the zero-force condition, there is the elastic unloading response of the pier. Therefore, the displacement corresponding to point 7, Δ_7 (*i.e.*, residual displacement), is given by:

$$\Delta_7 = \Delta_6 - F_6/k_E \tag{17}$$

Based on post-earthquake reconnaissance missions, it has been generally recognized that bridges with residual drifts lower than 1% can be easily repairerd[5]. It is noteworthy that this suggestion has been adopted in the Japanese Code[47] and considered in several research works[25, 35, 49]. In the present work, this value is assumed as a threshold value to identify the superior self-centering capacity of the PRC pier, and hence, the following inequality should be satisfied:

$$\Delta_7 / h \le 1\% \tag{18}$$

It is worth mentioning that the above-described formulation does not account for ED of concrete damage and degradation, geometric nonlinearities, and PT force loss. The influence of these limitations is discussed in *Section 6*.

2.2 Design criteria and procedure

The design process for PRC bridge piers is conventionally based on the design of an equivalent monolithic bridge pier (*i.e.*, similar dimensions and amount of steel rebars). The PRC pier is successively detailed with the PT bar and ED bars to obtain the expected superior cyclic performance (*i.e.*, stiffness, strength, and ductility comparable or superior to those of the monolithic pier and 'acceptable' residual drift). To achieve the design objectives, eight key design criteria are implemented for the PRC pier at the target drift: *1)* self-centering response with a low residual drift (< 1%[47]); *2)* sufficient ED capacity; *3)* roughly equivalent amount of steel; *4)* prevention of PT bar yielding; *5)* reliability of grouted duct connection; *6)* avoidance of ED bar premature fracture; *7)* mortar bed integrity; and *8)* increased lateral force capacity.

The initial post-tensioning force (F_{PT_ini}) and total energy dissipating force (F_{ED}) [Criteria (1) and (2)] affect the self-centering and ED capacities of the PRC pier and need to be properly tuned to obtain the desired cyclic performance.[12, 31] The recentering coefficient Λ_c, proposed by Guerrini *et al.*[40], is employed to evaluate both behaviors.

$$\Lambda_c = \frac{F_{ED}}{F_G + F_{PT\_ini}} \tag{19}$$

The recommended values of Λ_c to achieve a satisfactory damping and self-centering performance span between 0.11 and 0.60.[40] However, it is noteworthy that a high initial PT force increases the self-centering capacity of the PRC pier but also introduces high compressive stresses at the interface. To overcome this issue, Wang *et al.*[49] proposed an upper limit of the total axial ratio η_{tol} for piers with a ratio of ED bars lower than 1.5%, given by:

$$\eta_{tol} = \eta_G + \eta_P = \frac{F_G + F_{PT\_ini}}{f_c A_g} \le 25\% \tag{20}$$

where η_G and η_P are respectively the axial ratios of gravity force and the initial PT force; and f_c is the cylinder strength of concrete, which equals to 0.79 cube strength of concrete f_{cube}.[12]

The PRC pier has similar dimensions to the equivalent monolithic pier and hence a similar amount of concrete. Also, the steel amount (including transversal and longitudinal) should be similar for a cost-effective design [Criterion (3)]. The volumetric ratio of transverse reinforcement between the monolithic pier and the PRC pier should not vary significantly; thus, the amount of longitudinal bar of two piers can be defined as follows:

$$A_{ED\_tot} + A_{PT\_tot} = A_{mon\_l} \tag{21}$$

where A_{mon_l} is the amount of longitudinal bar in the monolithic model; A_{ED_tot} and A_{PT_tot} are, respectively, the total amount of the ED and PT bars, which can be calculated as follows:

$$A_{ED\_tot} = F_{ED} / f_{u\_ED} \qquad A_{PT\_tot} = F_{PT\_ini} / f_{PT\_ini} \tag{22}$$

where f_{u_ED} and f_{PT_ini} are respectively the ultimate tensile strength of the ED bars and the initial PT stress of the PT bar. Note that at the target drift, the stress in the PT bar (f_{PT}) should be lower than the yielding threshold f_{y_PT} to preserve the self-centering capacity [Criterion (4)]. Therefore, f_{PT_ini} should be checked to meet the following condition:

$$f_{PT} = f_{PT\_ini} + E_{PT} \frac{\Delta_{PT}}{L_{PT}} \le f_{y\_PT} \tag{23}$$

Furthermore, once the properties of the PT and ED bars are designed, Eq. (18) should be used to quantitatively check the self-centering behavior.

Grout-filled ducts are incorporated in pier-to-footing connections of PRC piers [Figure 1(A)]. The anchorage length of ED bars (L_{ac}) inserted into the ducts [Criterion (5)] is defined according to the AASHTO provisions[1] as follows:

$$L_{ac} \ge 0.3 d_{ED} f_{y\_ED} / \sqrt{f_g} \tag{24}$$

where d_{ED} is the diameter of the ED bars and f_g is the compressive strength of high-strength grout. In addition, as shown in Figure 2(D), an unbonded length L_u is deliberately designed in the ED bars at the pier-footing interface to avoid the stress concentration and premature bar fracture at this location due to repeated joint opening and closing [Criterion (6)]. L_u is determined according to Bu *et al.*[30]. The material of the mortar bed should be selected to have sufficient compressive strength and toughness to accommodate rocking rotation demands without suffering local damage at the rocking toe [Criterion (7)].[11] Last, based on the above design parameters, the load capacity of the PRC pier [*i.e.*, F_4 in Figure 1(C)] is calculated through the developed analysis equations to check Criterion (8).

3. EXPERIMENT DESIGN AND TESTING

3.1 Case study bridge pier

A single-pier highway simply supported bridge is used for case study purposes. The selected bridge is assumed to be located in the southwest high seismicity region of China (Seismic design category C and Site class I) and designed according to the JTG/T B02-01-2008[50] and JTG B02-2013[51] specifications. A 5% damped designed spectrum with a peak horizontal acceleration equal to 0.71 g was used in the design. The bridge consists of a three-cell RC box girder with monolithic RC circular piers and a bent cap integral to the superstructure, having a total tributary weight of 7280 kN. The detailed geometry and configuration of the prototype structure are shown in Figure 3(A). The RC circular pier has a section diameter of 2.1 m and a height from the base to the gravity center of the superstructure of 9.5 m, giving an aspect ratio of 4.55. The pier's longitudinal reinforcing ratio is 1.32% (36-D40, *i.e.*, thirty-six 40 mm-diameter steel bars), and the transverse reinforcement is composed of a D18 spiral stirrups with a center to center spacing of 80 mm, corresponding to a volumetric reinforcing ratio of 0.64% [Section A-A in Figure 3(A)]. Pushover analysis of the prototype pier was conducted in a fiber-based OpenSees[52] model. The ultimate drift (due to the crushing of the concrete core) and base shear capacity of the prototype pier were 3.4% and 2453.7 kN, respectively. The key properties of the monolithic prototype pier are summarized in Table 1.

A scaled-down monolithic model [Figure 3(B)] of the prototype was defined through similitude analysis.[53] The scale factors for length (S_l) and stresses (S_σ) were respectively equal to 1/4.75 and 1. Scale factors of other physical quantities were obtained through similitude relations (*e.g.*, scale factor of force $S_F = S_\sigma \times S_l^2 = 1/4.75^2$).[53] The monolithic model consists of a 1/4.75 scale representation of the prototype with an axial gravity force (F_G) of 323 kN, a clear height of 1.75 m, and a section depth of 0.44 m (Table 1). The longitudinal reinforcement of the pier body is composed of 11-D16 (reinforcing ratio = 1.45%), while the transverse reinforcement is made of D8 spiral hoops spaced 60 mm, providing a volumetric reinforcing ratio of 0.84% [Section B-B in Figure 3(B)]. The design of the reinforcing layout in the monolithic model aimed to reproduce the cyclic performance of the prototype pier, which was validated by the comparison of their pushover capacity results, as shown in Table 1. It should be noted that the lateral force of the prototype in Table 1 should be scaled with the factor S_F and then compared with the pushover results of the monolithic model. The bent cap was down-scaled to the dimensions of 2400 × 740 × 500 mm [Section C-C in Figure 3(B)]. The detailed design parameters of the monolithic pier model are listed in Table 1. It is worth mentioning that the monolithic model was not experimentally tested, while its design served as a reference for the design of the PRC benchmark model.

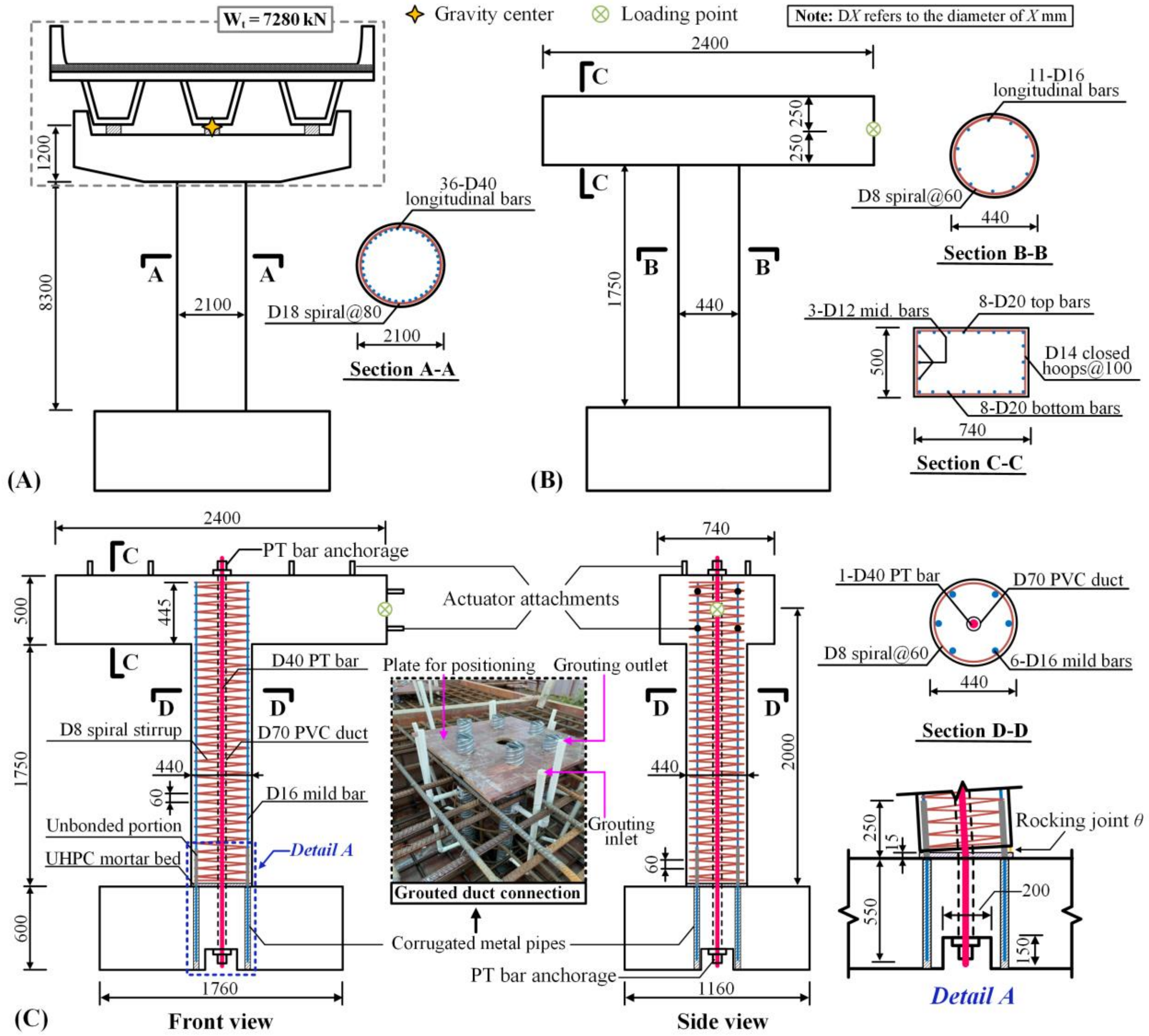

FIGURE 3 Schematic view: (A) Monolithic prototype structure; (B) monolithic scaled-down model; and (C) Test PRC benchmark model. [all dimensions are in mm].

TABLE 1 Design parameters for monolithic and PRC benchmark models.

Design Parameter	Monolithic: prototype	Monolithic: model	PRC benchmark: model
Pier diameter (m)	2.1	0.44	0.44
Pier clear height (m)	8.3	1.75	1.75
Pier cantilever height (m)	9.5	2.0	2.0
Axial gravity load (kN) [ratio (%)]	7280 [7.5]	323 [7.5]	323 [7.5]
Longitudinal reinforcing steel [ratio (%)]	36-D14 [1.32]	11-D16 [1.45]	6-D16 [0.79]
Transverse reinforcing steel [ratio (%)]	D18@80 [0.64]	D8@60 [0.84]	D8@60 [0.84]
PT steel [ratio (%)]	***	***	1-D40 [0.82]
Initial PT force (kN) [ratio (%)]	***	***	749 [17.5]
Longitudinal reinforcing + PT steel ratio (%)	1.32	1.45	1.61[a]
Ultimate drift (%)	3.4	3.6	≥3.6[b]
Base shear capacity (kN)	2453.7	108.2	≥108.2[b]

[a] Slightly larger than the target value of 1.45; [b] Design target values rather than the actual load and displacement capacity.

3.2 Test specimen matrix

The test matrix included six PRC rocking models at 1/4.75 scale of the prototype dimensions. The PRC benchmark model was designed to achieve a similitude with the monolithic model. Additional five specimens with different values of some design parameters were further constructed and experimentally investigated to evaluate the effect of these parameters on the pier's cyclic performance and provide insights into the adequacy of the design procedure.

The geometric dimensions for the PRC benchmark model were held constant compared to the monolithic model, as presented in Figure 3(C) and Table 1. To ensure an identical aspect ratio as the prototype structure (*i.e.*, 4.55), the lateral force in the scaled model was applied at the mid-height of the bent cap. The foundation had dimensions of 1760 × 1160 × 600 mm and was designed according to capacity design rules with respect to the actions transferred by the pier.[1, 2] The upper limits of the design parameters, $\Lambda_c = 0.6$ and $\eta_{tol} = 0.25$, were selected for the PRC benchmark model. Hence, according to the design criteria and procedure described in *Section 2.2*, the key design parameters of the PRC benchmark model were selected as F_{PT_ini} = 749 kN, F_{ED} = 643 kN, A_{ED_tot} = 1191 mm^2, and A_{PT_tot} = 1020 mm^2 (assuming f_{ED_u} = 540 MPa[54]). Considering the available standard sizes of mild and prestressing steel bars from suppliers, 1-D40 (1256 mm^2; ρ_{PT} = 0.82%) and 6-D16 (1206 mm^2; ρ_{ED} = 0.79%) were selected for the PT bar and ED bars, respectively. The resulting steel amount was slightly larger than that used in the monolithic model but within an acceptable range. Section D-D of Figure 3(C) shows the 440-mm diameter RC cross-section, including the 70 mm-diameter PVC pipe, placed at the center of the cross-section to serve as the ungrouted duct for the 1-D40 PT bar, the 6-D16 ED bars, and the D8 transverse spirals at 60 mm pitch. Table 1 lists the final dimensions, post-tensioning, and reinforcing details of the PRC benchmark model. Moreover, corrugated galvanized metal ducts with nominal diameter and wall thickness of 60 mm and 0.45 mm, respectively, and conforming to DG/TJ 08-2160-2015,[55] were used in the footing and subsequently filled with non-shrinkage high strength grout. The anchorage length (L_{ac}) for the grout-filled duct connection and the unbonded length (L_u) of ED bars were 550 mm and 250 mm, respectively, in which f_g and f_{y_ED} were respectively specified as 90 MPa and 400 MPa for design[54]. A 15-mm thick ultra-high performance concrete (UHPC) mortar bed was cast between the precast pier end and adjoining footing for construction tolerances according to the recommendation of Shen *et al.*[12, 13] Based on these design parameters, the f_{PT} at the target drift of 3.6% (*i.e.*, the ultimate drift of monolithic model) was calculated to be 889.3 MPa (≈ 0.80f_{y_PT}), with an adequate margin accounting for uncertainties on material properties. Figure 4(A) shows the analytical lateral force-drift behavior of the PRC benchmark model (highlighted in bold if not specifically stated), defined according to the formulation of *Section 2.1* and characterized by a base shear capacity at the target drift of 151.1 kN (>108.2 kN) and a residual drift of 0.03% (≈ 0).

The other five PRC pier specimens have the same dimensions as the benchmark one and were detailed by varying: *1)* the amount of ED bars; *2)* the initial PT force; and *3)* the unbonded length L_u in ED bars. The values of design parameters are reported in Table 2. To facilitate interpretation, the notation of 'PRC-Pη_P(%)Eρ_{ED}(%)' is used to identify specimens with different ratios of initial post-tensioning η_P and ED bars ρ_{ED}. For the specimen without the unbonded length of ED bars, the '-U0' is added at the end of the notation. The comparisons of the analytical force-drift response between these PRC specimens are shown in Figure 4. Figures 4(A) and (B) illustrate the influences of ED bar amount and PT force variations, respectively. As expected, enhanced lateral load and energy dissipation capacities are obtained by increasing the amount of ED bars. It can be observed that the initial PT force controls the lateral load capacity of the PRC pier; however, no significant differences were observed in terms of self-centering capacity due to the large initial PT force provided even at the least PT force level. The difference in the analytical hysteretic loops between the cases with and without the ED bars' unbonded length is shown in Figure 4(C). It can be observed that the ED bars' unbonded length could mitigate the unloading stiffness degradation due to the smaller plastic deformations of ED bars. Moreover, it is noteworthy that all PRC specimens are characterized by the same post-elastic stiffness (*i.e.*, after yielding of all ED bars), indicating that this parameter is independent of the variables investigated in this test matrix (*i.e.*, η_P, ρ_{ED}, and L_u) (see Eq.s 10(b) and 13(b) considering ED bars yielding).

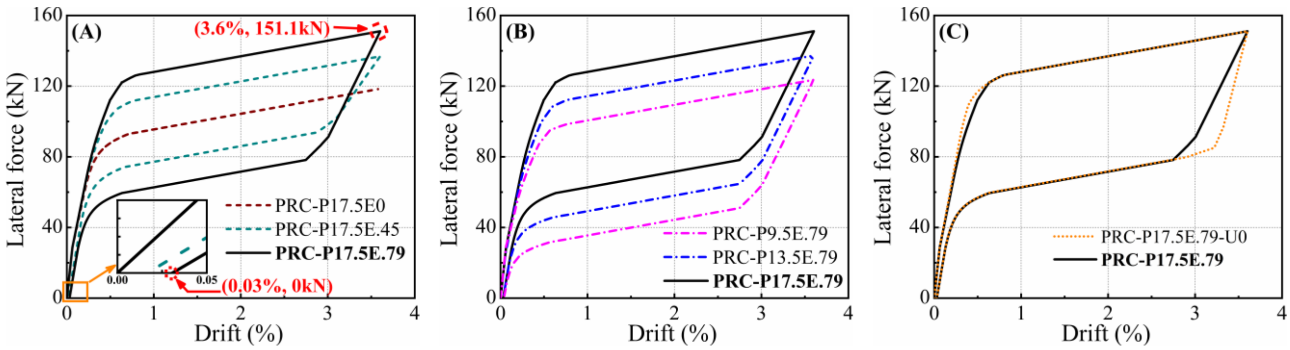

FIGURE 4 Analytical lateral force-drift behavior of PRC specimens with: (A) variation of ED bars amounts; (B) variation of initial PT forces; and (C) with and without unbonded length in ED bars.

TABLE 2 Test specimen matrix.

Specimen ID	Reinforcement		Post-tensioning			L_u (mm)
	ED bars	ρ_{ED} (%)	F_{PT_ini} (kN)	η_P (%)	F_{PT_ini}/F_{y_PT}[a]	
PRC-P17.5E0	***	0	749 [745[b]]	17.5	0.55	250
PRC-P17.5E.45	6-D12	0.45	749 [756[b]]	17.5	0.55	250
PRC-P17.5E.79	**6-D16**	**0.79**	**749 [746[b]]**	**17.5**	**0.55**	**250**
PRC-P13.5E.79	6-D16	0.79	579 [584[b]]	13.5	0.43	250
PRC-P9.5E.79	6-D16	0.79	409 [412[b]]	9.5	0.30	250
PRC-P17.5E.79-U0	6-D16	0.79	749 [764[b]]	17.5	0.55	***

[a] F_{y_PT} is the yielding force of the PT bar (*i.e.*, $f_{y\_PT} \times A_{PT}$ = 1356.5 kN); [b] The actual (effective) initial PT force before testing.

3.3 Material properties

Five different materials were used in the PRC models: *1)* conventional concrete; *2)* UHPC; *3)* high-strength grout; *4)* reinforcing steel [stirrup and ED bars]; and *5)* PT bar. The mechanical properties of the concrete (including grout) and the steel (including PT bar) are listed in Tables 3 and 4, respectively. Twelve conventional concrete samples, *i.e.*, six cubes and six rectangular prisms respectively for compressive strength and elastic modulus, were cast during the construction of the models. Note that the PRC-P17.5E.79-U0 was cast from another batch of concrete with the same mix proportions, and its properties are listed in the square bracket in Table 3. The UHPC for the mortar bed was composed of water, steel fiber (about 15 mm in length), and premix (including aggregates, cement, and filler materials) according to the following proportions 2.32 kg: 2.1 kg: 25 kg developing a compressive strength of 134.4 MPa and an elastic modulus of 44.4 MPa. The high-strength grout used to fill corrugated ducts exhibited an average value compressive strength of 101.3 MPa and an elastic modulus of 39.6 MPa (obtained according to Lim and Ha[56]). It is noteworthy that the PT bar's yield and ultimate strengths were close to the nominal values used for design; conversely, an overstrength of approximately 20% was observed for the strength of ED bars.

TABLE 3 Mechanical properties of the concrete and grout.

Material	Compressive strength test		Elastic modulus test	
	Sample dim. (mm)	Strength (MPa)	Sample dim. (mm)	*E* (GPa)
Conventional Concrete	150 × 150 × 150	f_{cu}, 35.9 [41.1[a]]	150 × 150 × 300	E_c, 32.7 [34.2[a]]
UHPC	100 × 100 × 100	f_{UHPC}, 134.4	100 × 100 × 300	E_{UHPC}, 44.4
High-strength grout	40 × 40 × 160	f_g, 101.3	***	E_g, 39.6[b]

[a] Only for specimen HRC-P17.5E.79-U0; [b] Elastic modulus of high-strength grout was calculated from $8500 f_g^{1/3}$.[56]

TABLE 4 Mechanical properties of the steel.

Material	Yielding stress (MPa)	Yielding strain ($\mu\varepsilon$)	Elastic modulus (GPa)	Ultimate stress (MPa)	Ultimate strain (%)	Fracture strain (%)
D8 stirrup	449.2	2144	209.5	684.9	10.3	16.5
D12 mild bar	544.6	2544	214.1	638.9	8.8	19.9
D16 mild bar	540.1	2475	218.2	681.6	10.7	21.9
D40 PT bar[a]	1067.7	4958	215.3	1116.6	9.5	20.5

[a] Middle portion of the coupons was machined down to 20 mm in diameter to ensure that the ultimate strength did not exceed the capacity of the testing equipment.

3.4 Test setup

The general layout of the experimental setup, including the instrumentations, is shown in Figure 5. The tributary gravity loads from the superstructure were applied through two vertical 150-ton hydraulic actuators, and the lateral load was applied in displacement control through one 50-ton horizontally-aligned hydraulic actuator [Figure 5(A)]. The two vertical actuators were free to move laterally by the slide rail hence maintaining the applied axial load of 300 kN (minus the mass of the bent cap, 2.31 ton) in the vertical direction during the tests. The instrumentations included string potentiometers, linear variable differential transformers (LVDTs), load cells, and strain gauges, as shown in Figure 5(A). The joint opening at the pier-footing interface was monitored by four vertical LVDTs on the four sides of the pier base. Curvatures within the pier bottom region within a height of 500 mm were measured using eight vertical downward LVDTs (*i.e.*, at a distance of 100 mm) on the west and east faces. Two longitudinal ED bars at both the pier' extreme west and east faces [Section A-A in Figure 5(A)] were monitored with strain gauges at four height levels: two within the unbonded portion and two within the bonded portion. Horizontal load in the lateral actuator was monitored by its built-in load cell, whereas a string potentiometer recorded the lateral displacement. In addition, a load cell positioned above the bent cap monitored the PT bar force throughout the test, while strain gauges were also placed along the PT bar. Figure 5(B) shows a photo of specimen PRC-P9.5E.79 and its test apparatus before testing.

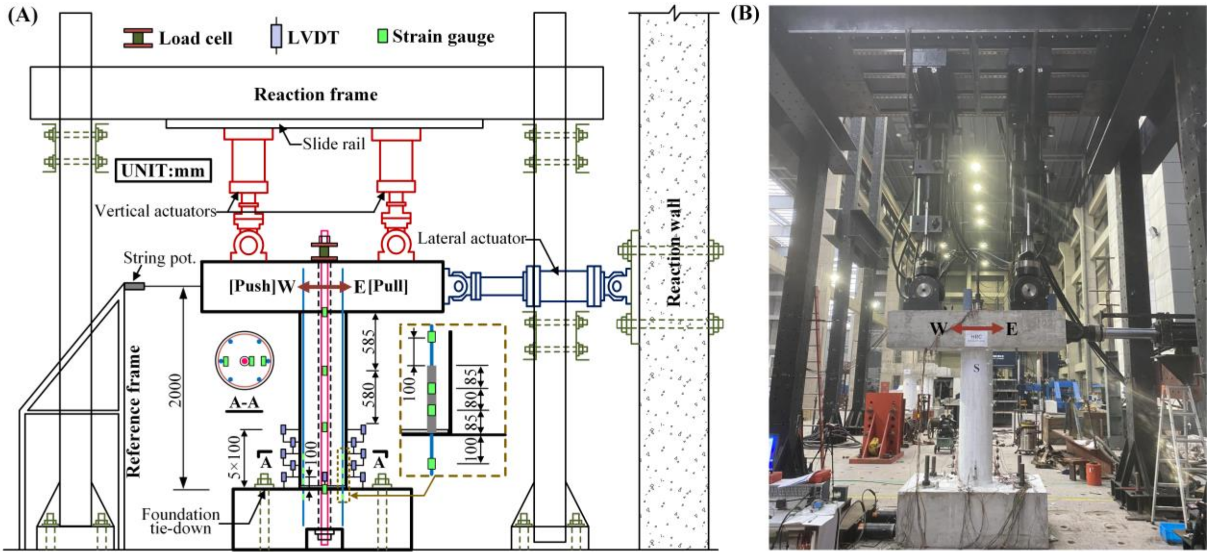

FIGURE 5 Test setup and instrumentation details: (A) Schematic representation; (B) Test facility photograph.

After the application of the axial force, the specimens were subjected to the identical displacement (drift)-control lateral cycle loading protocol, as shown in Figure 6. The first lateral displacement was imposed in the west direction [Figure 5(A)]. The loading protocol comprised 19 increasing drift levels (up to 4.8% drift) with each level repeated three times; however, the test of each specimen was terminated at different drift levels due to the different ultimate capacity. The first few cycles (up to 0.6% drift) were conducted with increasing steps of 0.1% drift to capture the drifts related to ED bars yielding. Successively, the cycles until 1.6% drift (corresponding to the moderate damage of concrete cover at the pier base) were conducted with increasing steps of 0.2% drift. The following cycles were conducted with increasing steps of 0.4% until concrete core crushing or/and ED bars fracture occurred.

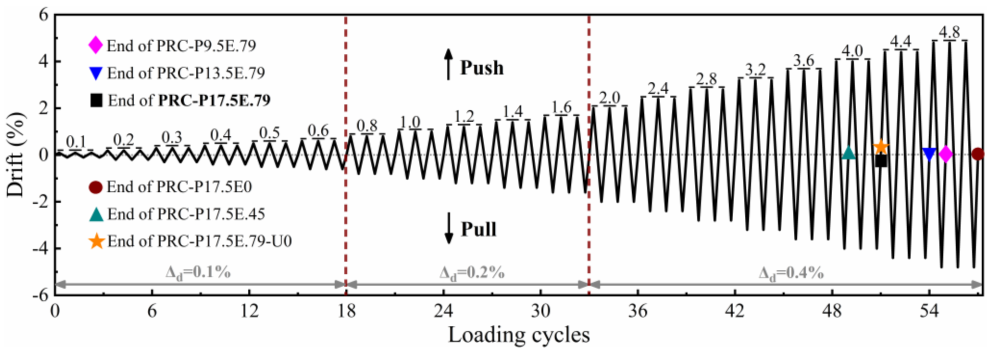

FIGURE 6 Lateral drift loading histories for tested specimens.

4. GENERAL PERFORMANCE ASSESSMENT AND TEST OBSERVATIONS

4.1 Hysteretic performance and damage observed

Figure 7 shows the cyclic response of the six PRC piers. Figures 7(A) to (C) show the cyclic responses of PRC-P17.5E0, PRC-P17.5E.45, and PRC-P17.5E.79. Their comparison demonstrates how the use of a large amount of ED bars can enhance the dissipation capacity, at the same time leading to larger residual drifts, hence reducing the self-centering capacity of the PRC pier. Figures 7(C) to (E) show the cyclic responses of PRC-P9.5E.79, PRC-P13.5E.79, and PRC-P17.5E.79. Their comparison demonstrates how the use of a low PT force leads to larger residual drifts and reduced lateral strength of the PRC pier. These trends are consistent with the analytical formulations of *Section 3.2*. More details on the parameters' influences are discussed in *Section 5*.

Five damage states were identified during the tests, defined as: *1)* onset of visible cracking, *2)* concrete cover spalling, *3)* exposure of steels, *4)* concrete core crushing, and *5)* ED bars fracture, and their evolution is indicated in Figure 7. The damage was concentrated at the pier bottom with concrete cover spalling, toe crushing, and ED bars buckling and/or fracture for all specimens. Few horizontal cracks were observed along the pier's bottom half, indicating that the pier flexural deformation was limited during the test (*i.e.*, rocking-dominant response).

Figure 7(C) shows the cyclic response of the benchmark pier (PRC-P17.5E.79), while Figure 8 shows its key damage status at selected drifts. The benchmark pier exhibited a flag-shape hysteretic response. A slight asymmetry in peak lateral strength and its corresponding drift was observed during the test due to concrete heterogeneity and construction tolerances (*i.e.*, peak strength equal to142.6 kN at 1.2% drift for the push direction and -128.5 kN at 1.0% drift for the pull direction). Initial cracks were detected at the pier-mortar bed interface at 0.2% drift [Figure 8(A)], which subsequently developed into the gap-opening mechanism. The flexural cracks of the pier shaft originated at the height of approximately 15 cm for drifts of 0.3% [Figure 8(A)]. ED bars reached the yield strain of 2475 $\mu\varepsilon$ for drifts of 0.6%. Minor concrete cover spalling was observed for drifts of 1.0% [Figure 8(B)] and gradually extended for increasing drifts amplitudes [Figure 8(C)], resulting in lateral strength and stiffness degradation. Cyclic loading continued leading to vertical cracks in the vicinity of the pier base on both sides and a noticeable gap-opening at the pier-mortar bed interface. As shown in Figure 8(C), for a drift of 2.0%, the gap-opening was approximately 4 mm. After completion of the 2.0% drift cycles, the stirrup at the west side of the pier was partially exposed while, at the east side, stirrup's exposure occurred at the subsequent drift of 2.4% [Figure 8(D)]. The test was terminated at 4.0% drift due to ED bars fracture and concrete core crushing on the west side, and ED bars buckling on the east side [Figure 8(E)]. Concrete cover damage was within a height of approximately 25 cm, and no damage was observed in the UHPC mortar bed.

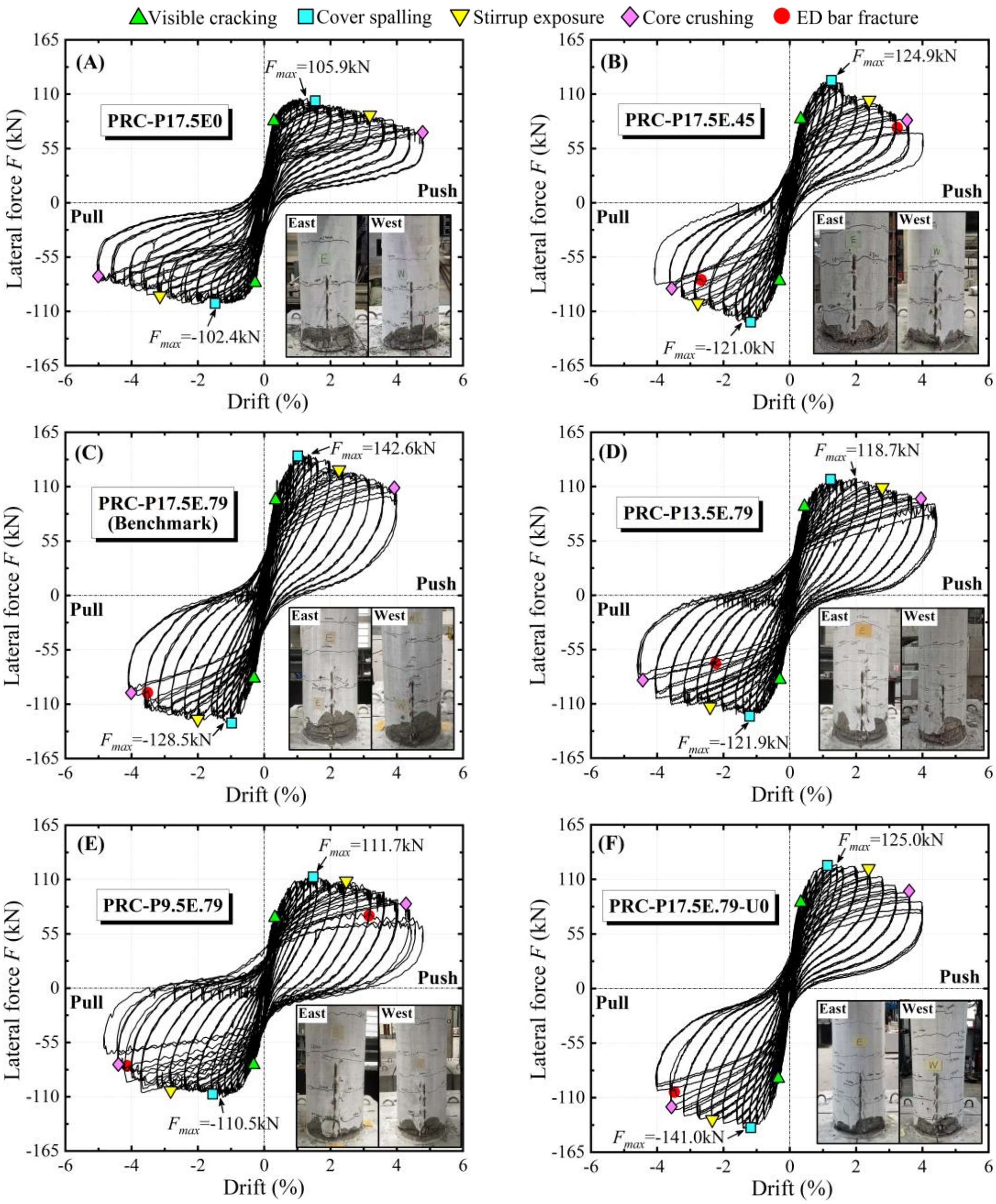

FIGURE 7. Experimental lateral force vs. drift for: (A) PRC-P17.5E0; (B) PRC-P17.5E.45; (C) PRC-P17.5E.79 [*i.e.*,

benchmark pier]; (D) PRC-P13.5E.79; (E) PRC-P9.5E.79; and (F) PRC-P17.5E.79-U0.

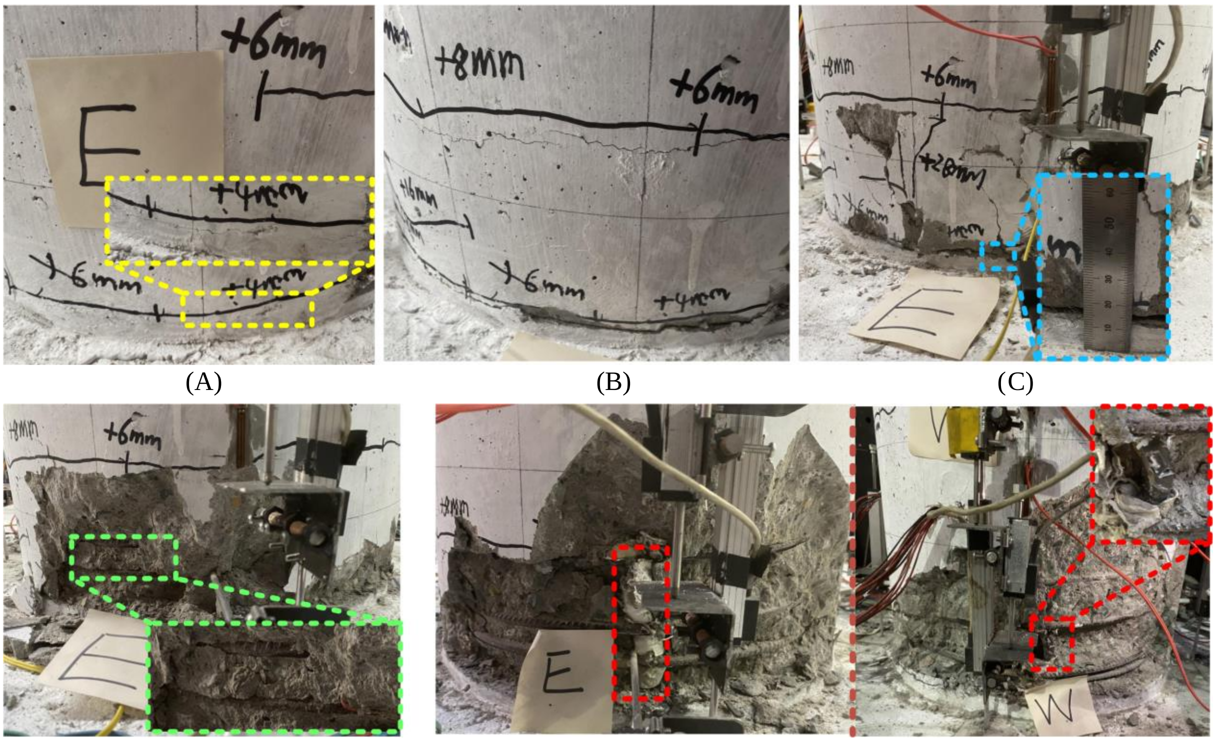

(A) (B) (C)

(D) (E)

FIGURE 8 Damage progression of PRC-P17.5E.79 (*i.e.*, benchmark pier) at: (A) 0.3% drift; (B) 1.0% drift; (C) 2.0% drift; (D) 2.4% drift; and (E) 4.0% drift. [grid size:10 cm × 10 cm].

Figures 7(A) and (B) show the cyclic response of PRC-P17.5E0 and PRC-P17.5E.45. It can be observed that peak forces were lower compared to the benchmark pier (*i.e.*, PRC-P17.5E.79) due to the reduced amount of ED bars. Significant concrete damage extending up to approximately 20 cm from the rocking joint (comparable to PRC-P17.5E.79) also occurred at the bottom of these two piers. It is worth highlighting that although ED bars were not included in PRC-P17.5E0, a flag-shape hysteretic response with small residual drifts was still observed in this system [Figure 7(A)]. This is in contrast with the expected non-linear elastic response shown in Figure 4(A), defined according to the analytical formulation. In this case, the moderate energy dissipation observed in Figure 7(A) is related to concrete damage at the pier base, and hence the discrepancy between the experimental and analytical results is related to the assumptions made in the analytical formulation, which does not account for concrete damage and degradation. It is worth mentioning that a more significant strength and stiffness degradation was observed for PRC-P17.5E.45 for drifts exceeding 1.2% [Figure 7(B)]. This was primarily caused by the imperfections during the construction of the specimen (*i.e.*, slight inclination or bending of ED bars). As a result, this potential flaw also rendered the fracture of ED bars easier in PRC-P17.5E.45, which occurred at a drift of 3.6%. Figures 7(D) and (E) show the cyclic response of PRC-P13.5E.79 and PRC-P9.5E.79. For these two cases, the extent of damage at the pier base was relatively minor compared to the benchmark pier (*i.e.*, PRC-P17.5E.79) due to the lower initial PT force. Concrete spalling was observed in the region with a height of 15 cm and 10 cm, respectively, in PRC-P13.5E.79 and PRC-P9.5E.79. The lower PT force also slightly delayed the onset of concrete spalling, which occurred after drifts of 1.0%. Figures 7(F) shows the cyclic response of PRC-P17.5E.79-U0 (*i.e.*, benchmark pier w/o unbonded length). The response of this pier was similar to the benchmark pier (*i.e.*, PRC-P17.5E.79), including damage visual observations and drift values related to ED bars fracture. Significant concrete cover spalling was observed for drifts larger than 2% resulting in ED bars' exposure and strain penetration effects, both simulating the unbonded length in PRC piers. Due to this debonding mechanism, the ED bars' fracture was observed for drifts of 3.6%, similar to the PRC-P17.5E.79 (*i.e.*, 4.0% drift). However, concrete cover deterioration was slightly less extensive in PRC-P17.5E.79-U0 than in PRC-P17.5E.79 due to the higher concrete strength (Table 3).

It is worth mentioning that no damage to the grouted corrugated duct connection, such as ED bars pullout, duct pullout, or conical failure of the footing, was observed in all PRC specimens. It is worth highlighting that only the base toes of PRC piers suffered concrete damage and that all columns were characterized by PT force loss during the tests (see Figure 10). These two effects resulted in the negative post-elastic stiffness (*i.e.*, softening) observed in the experimental force-drift plots, as opposed to the positive post-elastic stiffness (*i.e.*, hardening) determined by the analytical formulations (Figure 4). This aspect is further discussed in *Section 6*.

4.2 PT bar responses

Figure 9 shows the cyclic response of the PT force variation of the six PRC piers. Although the PT bars remained elastic, as observed by the strain gauges results (not shown here due to space constraints), the cyclic responses were characterized by PT force losses up to about 14%, mainly related to the concrete damage at the pier bases and the anchorage seating losses during the test. The PT stress losses increased for increasing drift values, as shown in Figure 10.

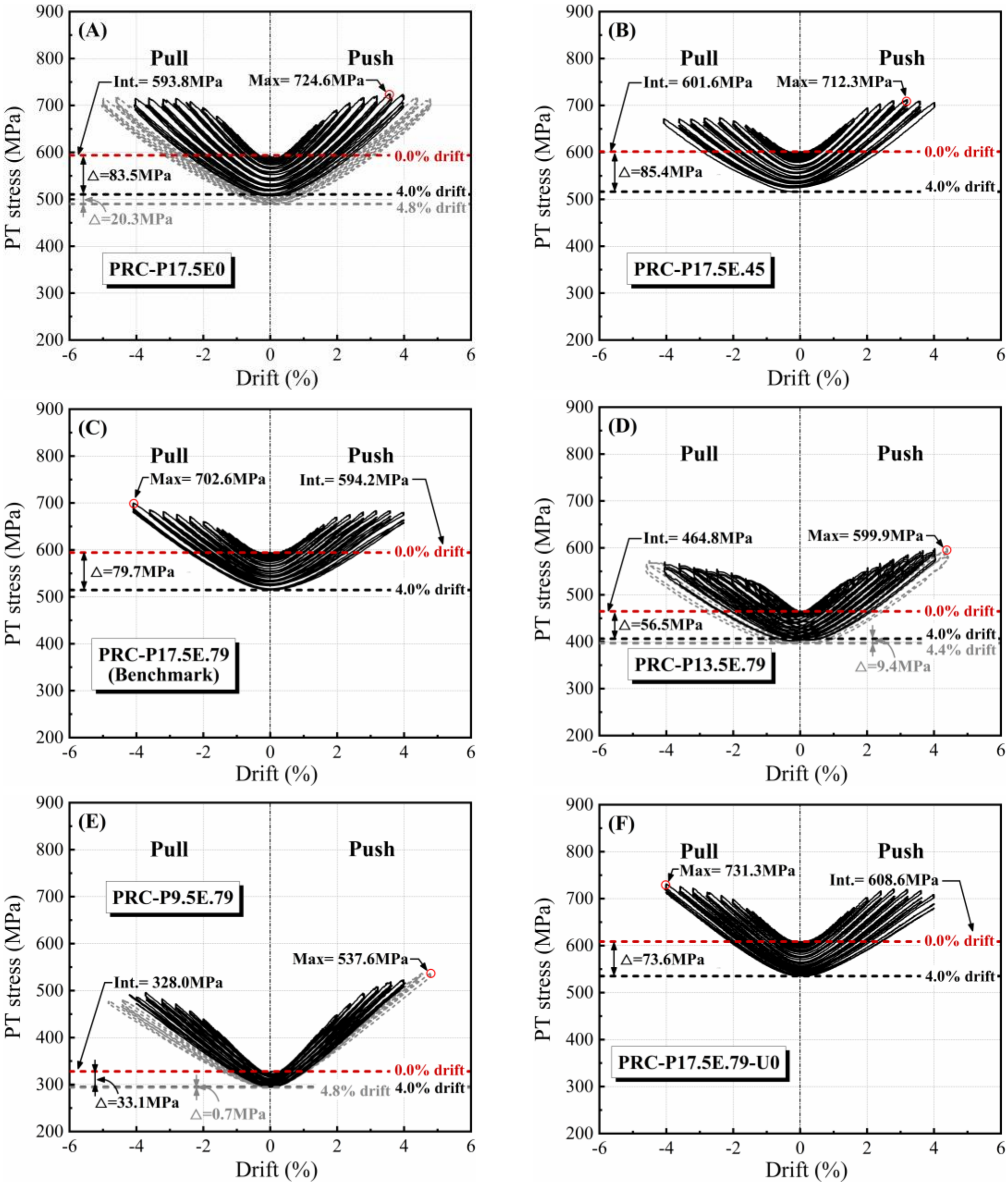

FIGURE 9 PT stress vs. drift for: (A) PRC-P17.5E0; (B) PRC-P17.5E.45; (C) PRC-P17.5E.79 [*i.e.*, benchmark pier]; (D) PRC-P13.5E.79; (E) PRC-P9.5E.79; and (F) PRC-P17.5E.79-U0.

Figures 9(A) to (C) show the cyclic response for piers PRC-P17.5E0, PRC-P17.5E.45, and PRC-P17.5E.79 (*i.e.*, benchmark) characterized by the same initial PT force. It can be observed that after completing the 4.0% drift amplitude, the PT stress values were respectively equal to 510.3, 516.2, and 514.5 MPa, corresponding to stress losses of 83.5, 85.4, and 79.7 MPa (*i.e.*, 14.1%, 14.2%, and 13.4% of the initial PT stress). A similar PT stress loss ratio (approximately 14%) in these three PRC piers was expected because their damage status and extent were similar, and the initial PT forces were comparable. Similar results were observed by Shen *et al.*[12]. Figures 9(C) to (E) show the cyclic response for piers PRC-P17.5E.79 (*i.e.*, benchmark), PRC-P13.5E.79, and PRC-P9.5E.79 characterized by a decreasing initial PT force. In this case, after completing the 4.0% drift amplitude, the PT stress values were respectively equal to 514.5, 408.3, and 294.9 MPa, corresponding to stress losses of 79.7, 56.5, and 33.1 MPa (*i.e.*, 13.4%, 12.2%, and 10.1% of the initial PT stress). It can be observed that a higher initial PT force results in a larger PT force loss ratio as a consequence of the higher compressive stress at the pier-footing interface and the consequent higher extent of concrete damage. Figure 9(F) shows the cyclic response of PRC-P17.5E.79-U0 (*i.e.*, benchmark pier w/o unbonded length), which was similar to the benchmark pier (*i.e.*, PRC-P17.5E.79). For all cases, the PT force loss results in a reduction of the lateral load capacity of PRC piers.[13] This effect, which was neglected in the analytical formulation of *Section 3.2*, contributes to the differences between the analytical and experimental results. Figure 10 shows that, for all PRC piers, the PT loss almost linearly increases while increasing the drift amplitudes. This trend allows accounting for the PT loss in the analytical formulation discussed in *Section 6*.

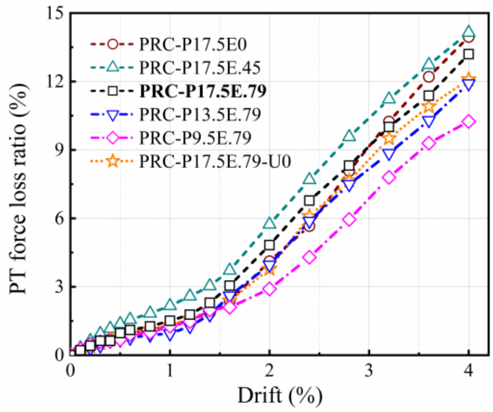

FIGURE 10 PT force loss ratio vs. drift.

5. COMPREHENSIVE PERFORMANCE ASSESSMENT FOR VARIOUS PARAMETERS

To comprehensively investigate the impact of ED bars amount, initial PT force, and ED bars unbonded length on the cyclic behavior of PRC models, detailed comparisons of measured results in terms of global hysteretic properties and local pier bottom responses are presented in this Section. The backbone curve, relative self-centering efficiency (RSE)[12] parameter, and equivalent damping ratio ξ_{eq} are selected to describe the pier's global hysteretic properties, while the neutral axis depth c and gap-opening d_{open} are used to describe the response at the pier's base section.

5.1 Properties of global hysteretic behavior

Figure 11 shows the average (considering the push and pull directions) backbone curves of the cyclic response as well as the corresponding idealized elasto-plastic curves[1, 2] with the failure condition defined by a lateral load capacity equivalent to 80% of the peak lateral load[14, 36]. The curves in Figures 11(A), (B), and (C) are grouped to facilitate the comparison of the different parameters investigated. Based on the idealized elasto-plastic curves, the key parameters for the force-drift responses are summarized in Table 5. Note that, despite the rapidly deteriorating post-elastic behavior in PRC-P17.5E.45, due to the construction imperfections discussed earlier, it can still provide useful information for the interpretation of the general trends. The initial stiffness of all piers is comparable (*i.e.*, 22400, 22700, 23800, 21800, 23700, and 24600 kN/m for PRC-P17.5E0, PRC-P17.5E.45, PRC-P17.5E.79, PRC-P13.5E.79, PRC-P9.5E.79, and PRC-P17.5E.79-U0, respectively) and similar to the elastic flexural stiffness of the pier shaft, *i.e.*, 22500 kN/m. This was expected as, during the gap-closed phase, the response of the piers is independent of the base connection details. However, some differences can be observed following the gap-opening mechanism, corresponding to lateral forces of approximately 30 kN, and the difference became evident with forces of approximately 60 kN, with the rocking behavior dominating the response. The pier lateral forces (*i.e.*, both F_y and F_p) increased with the amount of ED bars [Figure 11(A)] and the level of initial PT force [Figure 11(B)], as previously discussed. The comparison of PRC-P17.5E.79 and PRC-P17.5E0 shows that the drift ductility (*i.e.*, $\mu_d = \delta_u / \delta_y$) of the PRC pier (Table 5) decreases for increasing ED bars amounts, which is consistent with the experimental results of Ou[36]. PRC-P17.5E.45 is disregarded from this comparison as its ultimate behavior was significantly affected by constructions imperfections, as previously discussed. On the other side, it is noteworthy that the yield drift and drift ductility are not significantly affected by the initial PT force. Similar influence is also observed by Hieber *et al.*[17]. The results show only a slight reduction of μ_d from 6.9 to 6.0 for η_P varying from 17.5% to 9.5%. The lowest μ_d among all specimens is the one of PRC-P17.5E.45, which, despite the abovementioned construction imperfections, reached a ductility value equal to 5.2, which implies that all tested PRC models essentially had excellent ductility capacity. In this context, it is worth recalling that the benchmark (*i.e.*, PRC-P17.5E.79) PRC pier was designed for a target drift of 3.6% (Table 1), and its actual drift capacity was 3.97%.

As previously mentioned, no evident difference was observed in the response of the PRC-P17.5E.79 and PRC-P17.5E.79-U0. Accordingly, their average backbone and idealized elasto-plastic curves are similar [Figure 11(C) and Table 5]. In this PRC pier, the gap-opening induced strains and reinforcements slip, *i.e.*, strain penetration, in the ED bars. This slip, combined with the effect of load reversals, progressively damaged the bond along the bonded portion of the ED bars. Figure 12 shows that the strain distribution and progression in the ED bars around the interface for PRC-P17.5E.79 and PRC-P17.5E.79-U0 are similar, highlighting how the strain penetration in PRC-P17.5E.79-U0 contributes to the definition of an unbonded length. Due to large strain demands and friction against the surrounding concrete, strain gauges on the ED bars were partially lost after the 1.6% drift. For drifts larger than 2.0%, the base concrete cover started spalling and crushing, exposing the ED bars. Through this combination of effects, the lack of an unbonded length in PRC-P17.5E.79-U0 did not adversely affect the performance of the PRC pier.

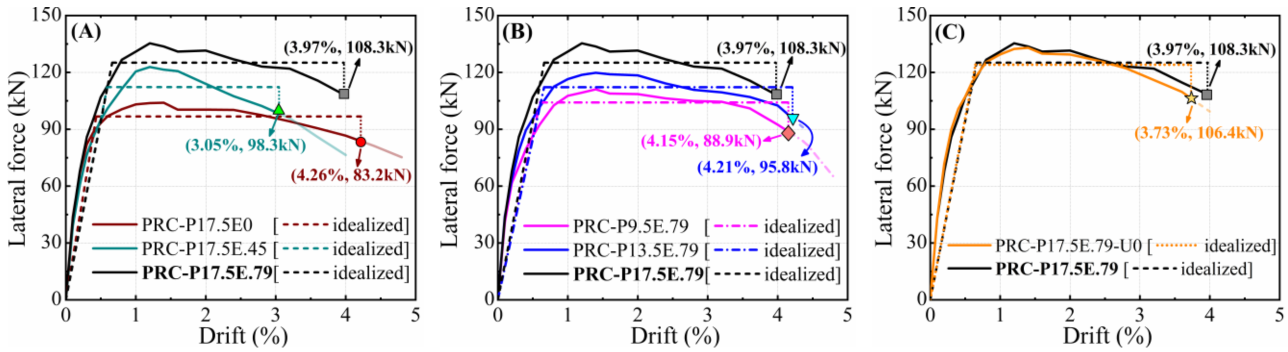

FIGURE 11 Comparison of average backbone curves for: (A) variation of ED bars amounts; (B) variation of initial PT forces; and (C) with and without unbonded length in ED bars.

Table 5 Elasto-plastic backbone curves parameters.

Specimen ID	δ_y (%)[a]	F_y (kN)[b]	Δ_p (%)[a]	F_p (kN)[b]	δ_u (%)[a]	F_u (kN)[b]	μ_d[c]
PRC-P17.5E0	0.44	96.7	1.40	103.9	4.26	83.2	9.8
PRC-P17.5E.45	0.59	112.3	1.20	122.9	3.05	98.3	5.2[d]
PRC-P17.5E.79	**0.66**	**125.1**	**1.20**	**135.4**	**3.97**	**108.3**	**6.0**
PRC-P13.5E.79	0.66	112.2	1.40	119.8	4.21	95.8	6.4
PRC-P9.5E.79	0.60	104.1	1.40	111.1	4.15	88.9	6.9
PRC-P17.5E.79-U0	0.65	124.0	1.40	133.0	3.73	106.4	5.8

[a] δ_y, δ_p, and δ_u refer to the equivalent yield, peak, and ultimate drift, respectively, where $\delta = \Delta/h$; [b] F_y, F_p, and F_u are the equivalent yield, peak, and ultimate force, respectively; [c] μ_d is the drift ductility coefficient, calculated as δ_u/δ_y; [d] ultimate response affected by construction imperfections.

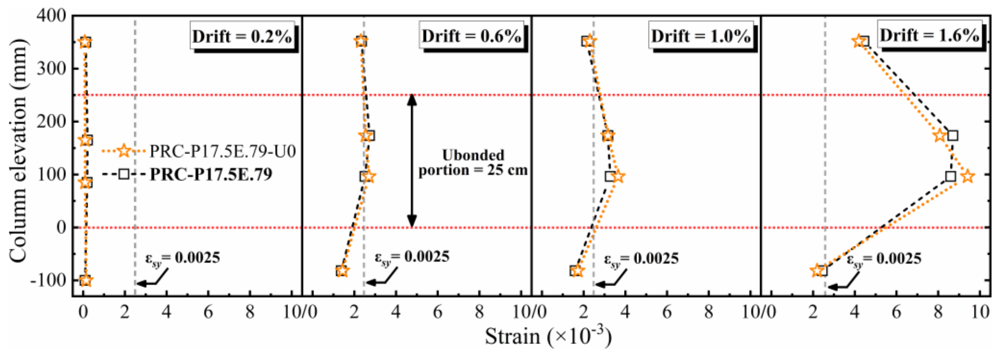

FIGURE 12 ED bars strain profiles of the PRC-P17.5E.79 and the PRC-P17.5E.79-U0.

Figure 13 shows the RSE values for the six piers and the different drifts amplitudes. The RSE represents the portion associated with recoverable drift in the imposed drift and is given by:

$$\mathrm{RSE} = 1 - \frac{\delta^{+}_{\mathrm{res}} - \delta^{-}_{\mathrm{res}}}{\delta^{+}_{\mathrm{peak}} - \delta^{-}_{\mathrm{peak}}} \tag{25}$$

where $\delta^{+}_{\mathrm{res}}$ and $\delta^{-}_{\mathrm{res}}$ are the residual drifts in the push and pull directions, respectively; and $\delta^{+}_{\mathrm{peak}}$ and $\delta^{-}_{\mathrm{peak}}$ are the imposed peak drifts in the push and pull directions, respectively. An RSE value of 1.0 means perfect self-centering capacity. For drift ratios up to 2.0%, all specimens showed a 'good' self-centering behavior with RSE values of 0.8-0.9. For larger peak drifts (exceeding 2.0%), significant differences can be observed among the RSE curves. Figure 13(A) shows the comparison of the RSE values considering the variability of the ED bars amount. The RSE values for PRC-P17.5E0 are about constant and equal to 0.9, while for PRC-P17.5E.45 and PRC-P17.5E.79, the RSE gradually decreases. The PRC model with a larger amount of ED bars (*i.e.*, benchmark PRC-P17.5E.79) experienced larger residual drift as a result of the concrete damage, PT force loss, and significant ED bars yielding. However, although the PRC-P17.5E.79 has a lower self-centering capacity, the residual drifts for the target drift of 3.6% are still lower than 1%[47]. Figure 13(B) shows the comparison of the RSE values considering the variability of the PT force. The results show that decreasing the initial PT force impairs the self-centering capacity of the PRC pier. For PRC-P9.5E.79 and PRC-P13.5E.79, the RSE values corresponding to 3.6% drift are respectively 0.44 and 0.65, leading to residual drift larger than 1%. It is noteworthy that, in contrast to the similar force capacity between PRC-P17.5E.79 and PRC-P17.5E.79-U0, their self-centering capacities extracted from the hysteretic curves were different when the imposed drift exceeded 2.0% [Figure 13(C)]. This was because the concrete cover significantly spalled in PRC-P17.5E.79 after 2.0% drift, but the higher concrete strength of PRC-P17.5E.79-U0 (Table 3) delayed the onset of this damage and reduced the extent. As a result, a higher RSE value was observed in specimen PRC-P17.5E.79-U0.

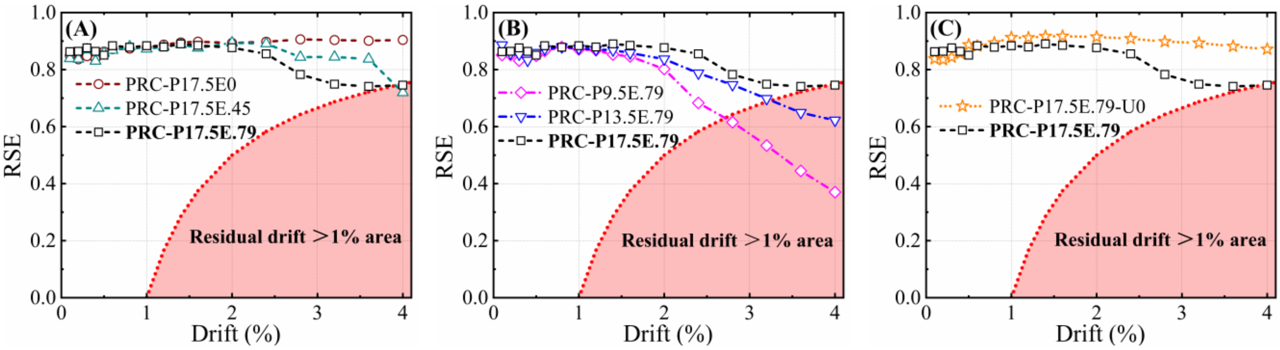

FIGURE 13 Comparison of RSE curves for: (A) variation of ED bars amounts; (B) variation of initial PT forces; and (C) with and without unbonded length in ED bars.

Figure 14 illustrates the ξ_{eq} variations among PRC piers with different parameters. No significant difference in terms of energy dissipation capacity is observed in the six PRC piers for drift values lower than 2%. For larger drifts, several differences can be observed. Figure 14(A) shows the comparison of the ξ_{eq} values considering the variability of the ED bars amount. The benchmark PRC-P17.5E.79 developed a higher damping ratio (ξ_{eq} up to 20%) compared with the other two piers with the lower ED bars amount, *i.e.*, about 1.4 and 1.2 times larger than the ξ_{eq} values of PRC-P17.5E0 and PRC-P17.5E.45, respectively, at the target drift (3.6%). Figure 14(B) shows the comparison of the ξ_{eq} values considering the variability of the PT force. A lower initial PT force results in a larger value of ξ_{eq}; thus, PRC-P9.5E.79 had the largest energy-dissipation capacity with ξ_{eq} up to 28% at the target drift (3.6%). The large ξ_{eq} value in PRC-P9.5E.79 is related to the larger gap-opening observed [discussed later, Figure 16(B)] and the larger ED bars elongation. PRC-P17.5E.79-U0 showed a slightly lower ξ_{eq} compared to the benchmark due to the different concrete strengths [Figures 14(C)].

Overall, based on the comparison results shown in Figures 13 and 14, the self-centering and ED capacities in the PRC pier had a conflicting trend with varying the parameters of interest; that is, increasing initial PT force or/and decreasing ED bars amount would promote the self-centering behavior but reduce the hysteretic energy-dissipation, especially for drifts larger than 2.0%, and vice versa. This phenomenon has also been corroborated by Shen *et al.*[12]

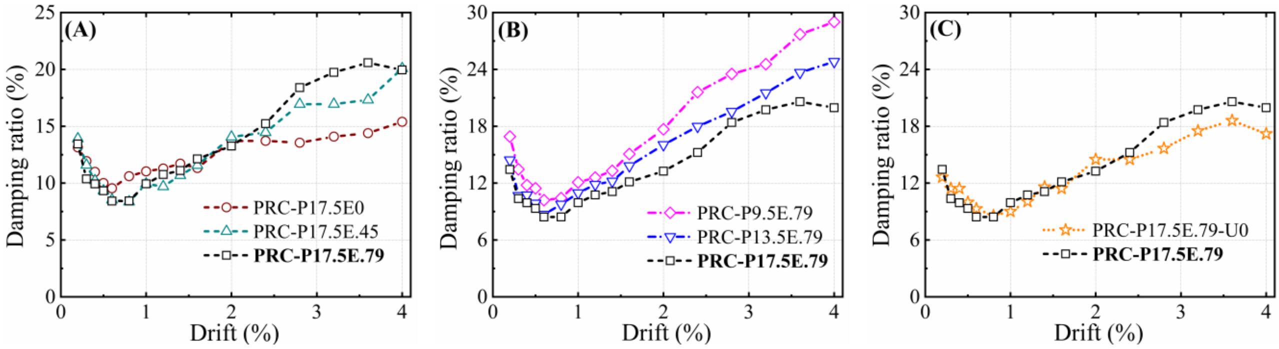

FIGURE 14 Comparison of equivalent damping ratio curves for: (A) variation of ED bars amounts; (B) variation of initial PT forces; and (C) with and without unbonded length in ED bars.

5.2 Local responses of the pier base

All PRC piers exhibited a rocking behavior where most of the deformation occurred at the pier's bottom end. The two main responses characterizing the rocking mechanism are related to the neutral axis depth c and the gap-opening d_{open}, which are shown in Figures 15 and 16, respectively. Figure 15 shows the neutral axis depth c normalized with respect to the pier diameter d. This parameter decreases rapidly to the value c/d = 0.50 with the onset of gap-opening, indicating that the PT bar would potentially elongate, and the restoring effect was activated. Increasing the base rotation/lateral drift, the neutral axis continued to move towards the contact edge of the cross-section with the minimum c/d (*i.e.*, c_{min}/d) of approximately 0.17, 0.23, 0.25, 0.20, 0.15, and 0.20 for PRC-P17.5E0, PRC-P17.5E.45, PRC-P17.5E.79, PRC-P13.5E.79, PRC-P9.5E.79, and PRC-P17.5E.79-U0, respectively, all occurring at a rotation of approximately 0.005. Thus, the assumptions in *Section 2.1.2* and Eq.s (4) that define an initial rocking state of $\theta = \theta_1$ and $c/d = 0.5$ and a critical rotation of 0.005 are validated by the experimental results for all the PRC configurations. However, it can be observed that the c_{min}/d value varies among the different piers and that the assumption of c_{min}/d constant and equal to 0.25 for $\theta > 0.005$ can only be taken as a rough approximation. Figure 15(A) shows the comparison of the c/d ratios considering the variability of the ED bars amount, while Figure 15(B) shows the comparison considering the variability of the PT force. The benchmark PRC-P17.5E.79 is characterized by the largest c_{min}/d value for $\theta > 0.005$. This is related to the larger reaction force at the base, and hence contact area, required in the PRC-P17.5E.79 to equilibrate the forces provided by the larger amount of ED bars and larger PT force. Lower values of c_{min}/d were observed while reducing the ED bars amount [Figure 15(A)] and the PT forces [Figure 15(B)]. The higher concrete resistance of PRC-P17.5E.79-U0 reduced the concrete damage hence leading to c_{min}/d values lower than those of PRC-P17.5E.79 [Figure 15(C)]. It is also worth mentioning that, as a consequence of the crushing of toe concrete and the loss of its partial vertical load-bearing capacity, a slight increase of the c/d value can be observed for large drifts (*e.g.*, $c/d = 0.38$ in the PRC-P17.5E.79 under the target drift). These results provide several insights but also show the need for advanced and optimized analytical formulations able to account for the variability of the ratio c/d to correctly represent the cyclic response of PRC piers.

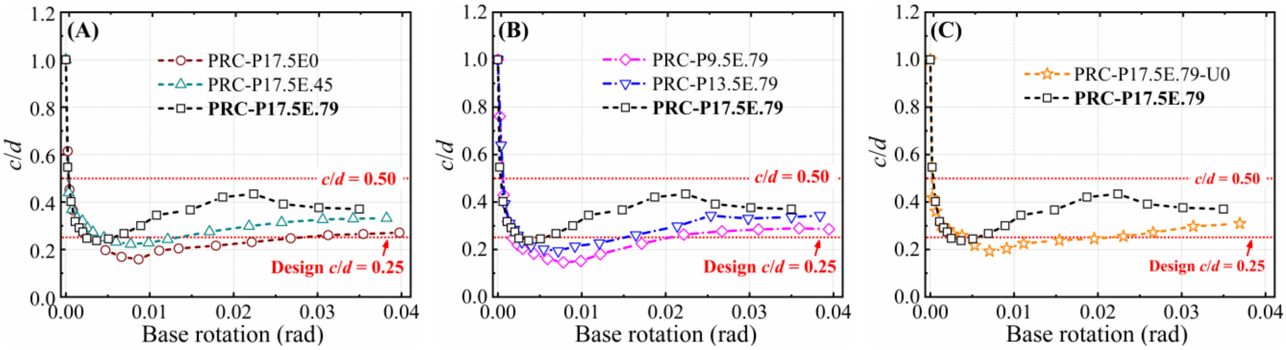

FIGURE 15 Comparison of neutral axis behavior for: (A) variation of ED bars amounts; (B) variation of initial PT forces; and (C) with and without unbonded length in ED bars.

Figure 16 shows the gap-opening behavior at the rocking interface. As a result of experiencing the largest c/d, the benchmark PRC-P17.5E.79 exhibited the smallest gap-opening. Figure 16 (A) shows the comparison of the gap-opening considering the variability of the ED amount. At the drift of 4.0%, the values of gap-opening in PRC-P17.5E.79 was 9.7 mm, which was about 0.76 and 0.86 times that of PRC-P17.5E0 and PRC-P17.5E.45, respectively. Figure 16(B) shows the comparison of the gap-opening considering the variability of the PT force. It can be observed that decreasing the initial PT force would trigger smaller compressive forces at the pier-mortar bed interface and consequently less contact area necessary to resist it. Also, a reduction of the neutral axis depth measured in PRC-P17.5E.79-U0 contributed to a slightly higher gap-opening in it compared to PRC-P17.5E.79 [Figure 16(C)].

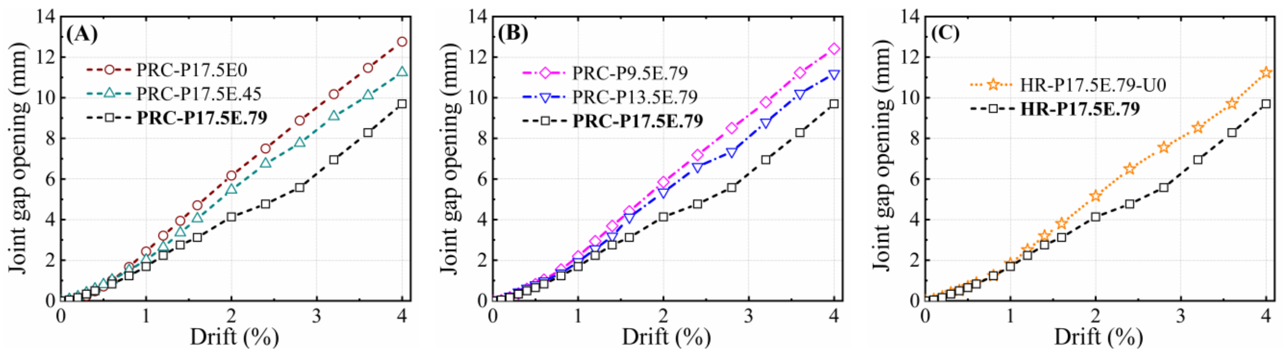

FIGURE 16 Comparison of joint gap-opening for: (A) variation of ED bars amounts; (B) variation of initial PT forces; and (C) with and without unbonded length in ED bars.

Based on the test results, it can be concluded that the PRC piers showed superior cyclic performance satisfying all design criteria presented in *Section 2.2*. However, some undesired effects were also observed, such as column spalling/crushing (affecting the ratio c/d) and the PT force loss, both to some extent reducing the PRC pier cyclic performance and introducing errors in the analytical evaluation of the force-drift relationship presented in *Section 2.1*.

6. COMPARISON OF TEST AND ANALYTICAL RESULTS

Based on the experimental results, two main differences can be observed with respect to the assumptions used in the analytical formulation presented in *Section 2.1*, *i.e.*, PT force loss (Figure 10) and the neutral axis depth variation (Figure 15). These differences have pronounced effects on force-drift behavior at large drifts, resulting in the obvious difference between the analytical (Figure 4) and experimental results (Figure 7). Consequently, the analytical equations presented in *Section 2.1* should be further optimized to reflect these two influence factors. Figure 17(A) shows the optimized c/d-θ curve, in which a linear trend with slope k_c is used to represent the c/d increasing after $\theta > 0.005$. The following equations are the optimized counterpart of Eq.s (4):

$$\left(\frac{c}{d}\right)_{\text{opt}} = \begin{cases} 1-k\theta & \theta \le \theta_1 \quad (k = 0.5/\theta_1) \\ \dfrac{A}{\theta}+B & \theta_1 < \theta < 0.005 \quad \left(A = \dfrac{0.005\theta_1 \times (0.5 - c_{\min}/d)}{0.005-\theta_1};\ B = \dfrac{0.005 \times c_{\min}/d - 0.5\theta_1}{0.005-\theta_1}\right) \\ c_{\min}/d + k_c(\theta - 0.005) & \theta \ge 0.005 \end{cases} \tag{28}$$

Note that upon unloading from the target rotation, as shown in Figure 17(A), the curve is assumed to follow a path parallel to the horizontal axis until it rejoins the curve of previously loading. This is because the damage to the base toe during loading is unrecoverable, and subsequent unloading only maintains this damage state until the gap-closed phase.

The PT force loss during the tests (Figure 10) compromised the PRC piers' lateral strength, and this effect can be reflected by a slope parameter k_{PT_loss}. As indicated in Figure 17(B), parameter k_{PT_loss} represents the slope between the PT force loss ratio and θ, and can be easily obtained from Figure 10 by linear regression. This regression can be used because, as mentioned before, an approximately linear trend was observed for these pier responses. By introducing k_{PT_loss}, Eq.s (5) that was used to calculate the PT force at the specific θ can be rewritten as:

$$(F_{PT})_{\text{opt}} = (1 - k_{PT\_loss}\theta) \times F_{PT\_ini} + A_{PT}E_{PT} \times \frac{\Delta_{PT}}{L_{PT}} \tag{29}$$

Based on the test results, Table 6 lists the neutral axis depth parameter c_{min}/d and k_c and the PT force loss parameter k_{PT_loss} for all PRC specimens. The coefficient of determination R_c^2 and $R_{PT\_loss}^2$, respectively for for k_c and k_{PT_loss}, are also given in Table 6. All R^2 values being close to 1 indicates that the linear regression can adequately describe the relationship between the optimized parameters and the rotation θ. It is worth mentioning that the optimized c/d - θ relationship should be further adjusted and validated against additional experimental tests considering other possible variables involved, *e.g.*, the dimensions of the PRC cross-section. Furthermore, this relationship is established for the circular cross-section and the evolution of the stress distribution at the PRC base could vary significantly for different sectional shapes; thus, the feasibility of the optimized c/d - θ relationship in the other shapes of the cross-section also requires more experimental investigation.

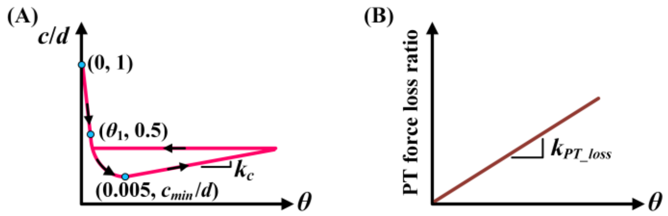

FIGURE 17 (A) Idealized c/d-θ relationship; (B) Idealized PT force loss ratio-θ relationship.

Table 6 Parameters in predicting force-drift response of six PRC models.

Specimen ID	c_{min}/d	k_c	R_c^2	k_{PT_loss}	$R^2_{PT\_loss}$
PRC-P17.5E0	0.17	5.3	0.945	3.2	0.978
PRC-P17.5E.45	0.23	4.7	0.951	3.6	0.997
PRC-P17.5E.79	**0.25**	**6.9**	**0.802**	**3.7**	**0.994**
PRC-P13.5E.79	0.20	4.9	0.914	3.3	0.989
PRC-P9.5E.79	0.15	4.8	0.906	2.4	0.984
PRC-P17.5E.79-U0	0.20	3.4	0.953	3.2	0.987

Figure 18 shows the comparison of experimental and analytical results for the PRC specimens in terms of lateral force-drift behavior at 4.0% drift. The backbone responses of the analytical models and the fitted c/d-θ curves [*i.e.*, Eq.s (28)] are also plotted in the figures. Note that ED bars' post-elastic hardening was considered in the analytical formulation and was defined based on the coupon tests. In general, the optimized analytical model is able to capture with reasonable accuracy the force-drift behavior of PRC piers, although the cycles from the experimental tests show larger energy dissipation. This is related to the additional mechanisms with respect to those represented by the analytical models, such as the ED bars' slip (*i.e.*, strain penetration), concrete damage, and/or potential PT localized contact to the duct edges inside the footing. The lack of consideration for these ED sources in the optimized analytical model resulted in the underestimation of the predicted residual drift. This effect is the most pronounced in the PRC-P17.5E0 [Figure 18(A)] that without ED bars. Some degree of errors between the experimental force values and the optimized analytical results were detected in the cases of PRC-P17.5E.45 [Figure 18(B)] and PRC-P17.5E.79-U0 [Figure 18(F)]. The inclination or bending of ED bars resulting from the construction imperfections and the debonding of ED bars due to base concrete spalling are, respectively, the causes of the prediction error for these two specimens. Both unfavorable factors resulted in the degradation of the accuracy of the analytical model. Additionally, it was observed that the uncalibrated analytical model would exaggerate the force resistance of piers, especially after the peak force. It should be noted that although the optimized analytical model follows the flag-shape with a reasonable prediction of force resistance, it cannot predict the strength and stiffness degradation of the PRC bridge piers under cyclic loading.

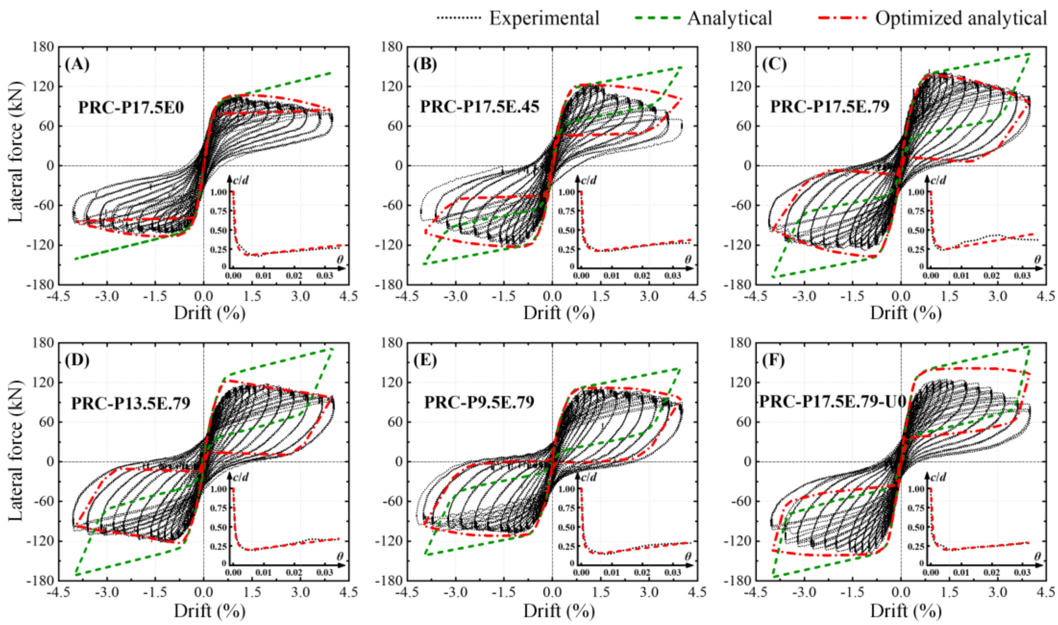

FIGURE 18 Comparison of force-drift behavior between experimental and analytical results at 4.0% drift for: (A) PRC-P17.5E0; (B) PRC-P17.5E.45; (C) PRC-P17.5E.79 (*i.e.*, benchmark pier); (D) PRC-P13.5E.79; (E) PRC-P9.5E.79; and (F) PRC-P17.5E.79-U0.

7. CONCLUSIONS

The present study focuses on the cyclic behavior of unbonded post-tensioned reinforced concrete (PRC) bridge piers subject to unidirectional quasi-static loading. According to specific performance criteria, a 1/4.75-scale PRC benchmark model was designed to exhibit superior cyclic performances with respect to a monolithic reinforced concrete (RC) bridge pier. Five other PRC version models were developed for assessing the influence of key design parameters. The investigated parameters were the amount of energy-dissipation (ED) bars, the initial post-tensioned (PT) force, and the absence of the unbonded length in the ED bars. An analytical formulation for the cyclic force-drift response of the PRC piers was defined and further calibrated and validated based on the test observations and results. The primary findings and conclusions from the investigations can be summarized as follow:

(1) The proposed PRC benchmark rocking pier (*i.e.*, PRC-P17.5E.79) met all expected design criteria with the lateral load and ultimate displacement capacities comparable or superior to the monolithic pier. Additionally, it exhibited a superior ED and self-centering behavior. Specifically, the PRC-P17.5E.79 model rocked in a controlled manner to an ultimate drift of approximately 4.0% with residual drift < 1.0% and a damping ratio ranging between 10% and 20%. However, the flag-shape cyclic response to some extent was related to concrete spalling/crushing and ED bars buckling/fracture, which were inevitable in PRC piers because of high compressive stress near the pier toes. This typical drawback led to an inaccurate evaluation of the ED capacity in some cases (*i.e.*, PRC-P17.5E0 model, w/o ED bars) and caused a non-negligible PT force loss in all cases.

(2) PRC piers with a larger amount of ED bars showed larger lateral force and ED capacity. On the other hand, a larger amount of ED bars reduces the self-centering behavior (*i.e.*, lower RSE values) and enlarges the interface contact area (*i.e.*, larger neutral axis depths) of the PRC piers, resulting in a smaller gap-opening.

(3) Varying the initial PT force played an essential role in the load-carrying, self-centering, and ED capacities of PRC piers but did not significantly influence their ductility capacity, all values of u_d being around 6.5. Increasing the level of initial PT force improved the self-centering behavior at the expense of the ED capacity. A larger

neutral axis depth was also observed for increasing initial PT forces. Moreover, higher initial PT forces result in larger compressive stress at the pier base, thus increasing the extent of the damage.

(4) Premature fracture of ED bars did not occur in the PRC pier without ED bars' unbonded length (*i.e.*, PRC-P17.5E.79-U0 model). This was due to the strain penetration at small drifts (< 2.0%) and the cover spalling and consequent exposure of the ED bars at large drifts (> 2.0%), which promoted debonding of the ED bars in the PRC-P17.5E.79-U0. Thus, except for a little difference in self-centering and ED capacities after 2.0% drift due to the slight concrete strength difference, the overall cyclic behavior between them was similar. This result suggests that could not be essential to design an ED bars' unbonded length, reducing construction complexity.

(5) The simple linear relationship can be used to describe both the variation of neutral axis depth and the PT force loss with increasing rotations. Thus, both effects were easily introduced into the developed analytical equations to strengthen the capacity of predicting the force-drift behavior of PRC piers.

(6) The developed relationship between c/d and θ is limited to the cross-section of the PRC piers tested in this study. It has been observed that the decompression points in the three PRC piers for different PT force are almost the same, inferring that a moderate variability of the axial force or cross-sectional size has small influence on the relationship between c/d and θ at the decompression stage. However, it has also been observed that there is a different evolution of c/d after the decompression point (*i.e.*, for $\theta > 0.005$) and the size of the column could play a role because of the different stress at the base *i.e.*, larger stress induces larger extension of damage of the contact surfaces at the base and hence, an increase of the c/d value. Thus, the evolution of c/d for θ values after the decompression point for different cross-sectional sizes, shapes, as well as the properties of the materials requires additional investigation to extend its general application.

(7) Overall, the unbonded PRC rocking bridge piers with well-designed parameters, such as a combination of η_P = 17.5% and ρ_{ED} = 0.79% in this study, is a good candidate for RC bridges constructed using accelerated construction techniques in regions of low to moderate seismicity; but for higher seismicities, the issue of concrete damage significantly emerges, violating the advanced design philosophy of minimal-damaged structures, and thus enhancement strategies for the integrity of the pier shaft or pier base are needed.

ACKNOWLEDGEMENTS

The financial support provided by the National Natural Science Foundation of China (Grant No. 51838010) is greatly appreciated by the authors. The first author also gratefully acknowledges the China Scholarship Council (Grant No. 202006260245) for financial support for the research visit at UCL.

REFERENCES

1. AASHTO. *AASHTO guide specifications for LRFD seismic bridge design*. Washington (DC): American Association of State Highway Transport Officials; 2015.
2. MOHURD. *Code for seismic design of urban bridge (CJJ 166-2011)*. Beijing: China Architecture and Building Press; 2011.
3. Shen Y, Li J, Freddi F, Igarashi A, Zhou J. Numerical investigation of transverse steel damper (TSD) seismic system for suspension bridges considering pounding between girder and towers. *Soil Dyn Earthq Eng*. 2022;155:107203.
4. Freddi F, Galasso C, Cremen G, Dall'Asta A, Di Sarno L, Giaralis A, Gutiérrez-Urzúa F, Màlaga-Chuquitaype C, Mitoulis SA, Petrone C, Sextos A, Sousa L, Tarbali K, Tubaldi E, Wardman J, Woo G. Innovations in earthquake risk reduction for resilience: recent advances and challenges. *Int J Disaster Risk Reduct*. 2021;60:102267.
5. Kawashima K, MacRae GA, Hoshikuma J, Nagaya K. Residual displacement response spectrum. *J Struct Eng*. 1998;124(5):523-530.
6. Wu S, Li H, Wang X, Li R, Tian C, Hou Q. Seismic performance of a novel partial precast RC shear wall with reserved cast-in-place base and wall edges. *Soil Dyn Earthq Eng*. 2022;150:107038.
7. Chen X, Li C. Performance of tall pier bridges retrofitted with lead rubber bearings and rocking foundation. *Eng Struct*. 2020;212:110529.
8. Elettore E, Lettieri A, Freddi F, Latour M, Rizzano G. Performance-Based Assessment of Seismic-Resilient Steel Moment Resisting Frames Equipped with Innovative Column Bases Connections. *Structures*. 2021;32:1646-1664.
9. Marriott D, Pampanin S, Palermo A. Quasi-static and pseudo-dynamic testing of unbonded post-tensioned rocking bridge piers with external replaceable dissipaters. *Earthq Eng Struct Dyn*. 2009;38:331-354.
10. Freddi F, Dimopoulos C, Karavasilis TL. Experimental evaluation of a rocking damage-free steel column base with friction devices.. *J Struct Eng*. 2020; 146(10): 04020217.
11. Tobolski MJ. *Improving the design and performance of concrete bridges in seismic regions*. PhD Dissertation, San Diego: University of California, 2010.
12. Shen Y, Liu X, Li Y, Li J. Cyclic tests of precast post-tensioned concrete filled steel tubular (PCFT) columns with internal energy-dissipating bars. *Eng Struct*. 2021;229:111651.
13. Shen Y, Freddi F, Li J. Experimental and numerical investigations of the seismic behavior of socket and hybrid connections for PCFT bridge columns. *Eng Struct*. 2022;253:113833.
14. Ou Y, Chiewanichakorn M, Aref AJ, Lee GG. Seismic performance of segmental precast unbonded posttensioned concrete bridge columns. *J Struct Eng*. 2007;133(11):1636-1647.

15. Mander JB, Cheng CT. *Seismic resistance of bridge piers based on damage avoidance design*. Technical Report NCEER-97-0014. NY, USA: University at Buffalo, State University of New York, 1997.
16. Cohagen LS, Pang JBK, Stanton JF, Eberhard MO. *A precast concrete bridge bent designed to re-center after an earthquake*. Research report No. WA-RD 684.3. University of Washington, Seattle, 2009.
17. Hieber DG, Wacker JM, Eberhard MO, Stanton JF. *Precast concrete pier systems for rapid construction of bridges in seismic regions*. Research report No. WA-RD 611.1. University of Washington, Seattle, 2005
18. Kwan WP, Billington SL. Unbonded posttensioned concrete bridge piers. I: monotonic and cyclic analyses. *J Bridge Eng*. 2003;8(2):92-101.
19. Kwan WP, Billington SL. Unbonded posttensioned concrete bridge piers. II: seismic analyses. *J Bridge Eng*. 2003;8(2):102-1011.
20. Palermo A, Pampanin S, Marriott D. Design, modeling, and experimental response of seismic resistant bridge piers with posttensioned dissipating connections. *J Struct Eng*. 2007;133(11):1648-1661.
21. Shim C, Chung C, Kim H. Experiments evaluation of seismic performance of precast segmental bridge piers with a circular solid section. *Eng Struct*. 2008,30:3782-3792.
22. Moussa AM, Fahmy FF, Wu Z. Innovative resilient system of precast segmental RC hollow bridge columns. *Eng Struct*. 2021,229:111555.
23. Hung H, Sung Y, Lin K, Jiang C, Chang KC. Experimental study and numerical simulation of precast segmental bridge columns with semi-rigid connections. *Eng Struct*. 2017,136:12-25.
24. Li C, Bi K, Hao H. Seismic performances of precast segmental column under bidirectional earthquake motions: Shake table test and numerical evaluation. *Eng Struct*. 2019;187:314-328.
25. Jia J, Zhang K, Wu S, Guo Y, Du X, Wang X. Seismic performance of self-centering precast segmental bridge columns under different lateral loading directions. *Eng Struct*. 2020;221:111037.
26. Thonstad T, Mantawy IM, Stanton JF, Eberhard MO, Sanders DH. Shaking table performance of a new bridge system with pretensioned rocking columns. *J Bridg Eng*. 2016;21(4):04015079.
27. Mantawy IM, Thonstad T, Sanders DH, Stanton JF, Eberhard MO. Seismic performance of precast, pretensioned, and cast-in-place bridges: Shake table test comparison. *J Bridg Eng*. 2016;21(10):04016071.
28. Li C, Hao H, Bi K. Numerical study on the seismic performance of precast segmental concrete columns under cyclic loading. *Eng Struct*. 2017;148: 373-386.
29. Chou C, Chang H, Hewes JT. Two-plastic-hinge and two dimensional finite element models for post-tensioned precast concrete segmental bridge columns. *Eng Struct*. 2013;46:205-217.
30. Bu Z, Ou Y, Song J, Zhang N, Lee GG. Cyclic loading test of unbonded and bonded posttensioned precast segmental bridge columns with circular section. *J Bridge Eng*. 2016;21(2):04015043.
31. Li Y, Li J, Shen Y. Quasi-static and nonlinear time-history analyses of post-tensioned bridge rocking piers with internal ED bars. *Structures*, 2021,32:1455-1468.
32. Pieroni L, Freddi F, Latour M. Effective placement of Self-Centering Damage-Free Connections for Seismic-Resilient Steel Moment Resisting Frames. *Earthq Eng Struct Dyn*. 2022. https://doi.org/10.1002/eqe.3615.
33. Li Y, Li J, Shen Y, Xu W. Cyclic behavior and simplified design method of hybrid rocking columns with external energy-dissipators. *J Earthq Tsunami*. 2020,14(6):2050026.
34. Roh H, Ou Y, Kim J, Kin W. Effect of yielding level and post-yielding stiffness ratio of ED bars on seismic performance of PT rocking bridge piers. *Eng Struct*. 2014;81:454-463.
35. Nikbakht E, Rashid K, Hejazi F, Osman S. A numerical study on seismic response of self-centring precast segmental columns at different post-tensioning forces. *Lat AM J Solids Struct*. 2014,11(5):864-883.
36. Ou Y. *Precast segmental post-tensioned concrete bridge columns for seismic regions*. PhD Dissertation. New York: State University of New York at Buffalo; 2007.
37. Zhang H, Geng X, Zhou W. Experiments on the hysteretic response of self-centering RC columns prestressed by unbonded posttensioned tendons. *J Earthqu Eng*. 2021. https://doi.org/10.1080/13632469.2021.1927908.
38. Fathi D, Okail H, Mahdi H, Abdelrahman A. Cyclic load behavior of self-centering hammer-head bridge. *AM J Eng Res*. 2018,7(1):88-89.
39. Ou Y, Wang P, Tsai MS, Chang KC, Lee GG. Large-scale experimental study of precast segmental unbonded posttensioned concrete bridge columns for seismic regions. *J Struct Eng*. 2010;136(3):255-264.
40. Guerrini G, Restrepo JI, Massari M, Vervelidis A. Seismic behavior of posttensioned self-centering precast concrete dual-shell steel columns. *J Struct Eng*. 2015;141(4):04014115.
41. Liu Y, Zhou W. Numerical modeling to predict seismic performance of the post-tensioned self-centering concrete shear walls. *Bull Earthq Eng*. 2022;20:1057-1086.
42. Aaleti S, Sritharan S. A simplified analysis method for characterizing unbonded post-tensioned precast wall systems. *Eng Struct*. 2009;31(12):2966-2975.
43. Felipe JP, Stephen P, Richard S. Seismic design of unbonded post-tensioned precast concrete walls with vertical joint connectors. *PCI J*. 2004;49(1):58-79.
44. Thomas DJ, Sritharan S. *An evaluation of seismic design guidelines proposed for precast jointed wall systems*. ISU-ERI-Ames Report ERI-04643. USA: Iowa State University, 2004.
45. Pampanin S, Priestley MJN, Sritharan S. Analytical modeling of the seismic behavior of precast concrete frames designed with ductile connections. *J Earthqu Eng*. 2001;5(3):329-367.
46. Raynor DJ, Lehman DE, Stanton JF. Bond-slip response of reinforcing bars grouted in ducts. *ACI Struct J*. 2002;99(5):568-576.
47. JRA. *Design specifications of highway bridges-Part 5: seismic design.* Tokyo: Japan Road Association; 2016.

48. Valigura J, Salehi M, Liel AB, Sideris P. Seismic repair assessment of hybrid sliding-rocking bridge columns through integrated experimentation and expert panel solicitation. *J Struct Eng*. 2020;146(9):04020191.
49. Wang Z, Wang J, Liu T. Axial compression ratio limit for self-centering precast segmental hollow piers. *Struct Concr*. 2017;18(5):668-679.
50. MOT. *Guideline for seismic design of highway bridges (JTG/T B02-01-2008)*. Beijing: China Communications Press; 2008.
51. MOT. *Specification of seismic design for highway engineering (JTG B02-2013)*. Beijing: China Communications Press; 2013.
52. OpenSees. *Open system for earthquake engineering simulation*. Pacific Earthquake Engineering Research Center, University of California, Berkeley, 2012.
53. Harris HG, Sabnis GM. *Structural modeling and experimental techniques (second edition)*. CRC Press; 1999.
54. MOHURD. *Code for design of concrete structures (GB 50010-2010)*. Beijing: China Architecture and Building Press; 2015.
55. Shanghai Housing and Urban Construction Management Committee. *Technical specification for prefabricated bridge piers (DGTJ 08-2160-2015)*. Shanghai: Tongji University Press; 2015.
56. Lim MK, Ha SS. Ultra-high-strength grout for filling steel pipes in offshore wind turbine. *Int J Appl Eng Res*. 2017; 12(23): 13064-13076.